

# Kepler's Supernova: An Overluminous Type Ia Event Interacting with a Massive Circumstellar Medium at a Very Late Phase

Satoru Katsuda<sup>1</sup>, Koji Mori<sup>2</sup>, Keiichi Maeda<sup>3,4</sup>, Masaomi Tanaka<sup>5</sup>, Katsuji Koyama<sup>6,7</sup>, Hiroshi Tsunemi<sup>6</sup>, Hiroshi Nakajima<sup>6</sup>, Yoshitomo Maeda<sup>1</sup>, Masanobu Ozaki<sup>1</sup>, & Robert Petre<sup>8</sup>

## ABSTRACT

We have analyzed *XMM-Newton*, *Chandra*, and *Suzaku* observations of Kepler's supernova remnant (SNR) to investigate the properties of both the SN ejecta and the circumstellar medium (CSM). For comparison, we have also analyzed two similarly-aged, ejecta-dominated SNRs: Tycho's SNR, thought to be the remnant of a typical Type Ia SN, and SNR 0509-67.5 in the Large Magellanic Cloud, thought to be the remnant of an overluminous (SN1991T-like) Type Ia SN. By simply comparing the X-ray spectra, we find that line intensity ratios of iron-group elements (IGE) to intermediate-mass elements (IME) for Kepler's SNR and SNR 0509-67.5 are much higher than those for Tycho's SNR. We therefore argue that Kepler is the product of an overluminous Type Ia SN. This inference is supported by our spectral modeling, which reveals the IGE and IME masses respectively to be  $0.95^{+0.34}_{-0.37} M_{\odot}$  and  $0.12^{+0.19}_{-0.05} M_{\odot}$  (Kepler's SNR),  $0.75^{+0.51}_{-0.15} M_{\odot}$

---

<sup>1</sup>Institute of Space and Astronautical Science (ISAS), Japan Aerospace Exploration Agency (JAXA), 3-1-1 Yoshinodai, Chuo, Sagamihara, Kanagawa 252-5210, Japan

<sup>2</sup>Department of Applied Physics and Electronic Engineering, Faculty of Engineering, University of Miyazaki, 1-1 Gakuen Kibanadai-Nishi, Miyazaki 889-2192

<sup>3</sup>Department of Astronomy, Kyoto University, Kitashirakawa-Oiwake-cho, Sakyo-ku, Kyoto 606-8502, Japan

<sup>4</sup>Kavli Institute for the Physics and Mathematics of the Universe (WPI), University of Tokyo, 5-1-5 Kashiwanoha, Kashiwa, Chiba 277-8583, Japan

<sup>5</sup>National Astronomical Observatory of Japan, Mitaka, Tokyo 181-8588, Japan

<sup>6</sup>Department of Earth and Space Science, Osaka University, 1-1 Machikaneyama-cho, Toyonaka, Osaka 560-0043

<sup>7</sup>Department of Physics, Graduate School of Science, Kyoto University, Kitashirakawa Oiwake-cho, Sakyo-ku, Kyoto 606-8502

<sup>8</sup>Astrophysics Science Division, NASA Goddard Space Flight Center, Greenbelt, MD 2077, USA

and  $0.34_{-0.25}^{+0.08} M_{\odot}$  (SNR 0509-67.5), and  $0.35_{-0.15}^{+0.55} M_{\odot}$  and  $0.70_{-0.28}^{+0.12} M_{\odot}$  (Tycho’s SNR). We find that the CSM component in Kepler’s SNR consists of tenuous diffuse gas ( $\sim 0.3 M_{\odot}$ ) present throughout the entire remnant, plus dense knots ( $\sim 0.035 M_{\odot}$ ). Both of these components have an elevated N abundance (N/H $\sim 4$  times the solar value), suggesting that they originate from CNO-processed material from the progenitor system. The mass of the diffuse CSM allows us to infer the pre-SN mass-loss rate of the system to be  $\sim 1.5 \times 10^{-5} (v_w/10 \text{ km s}^{-1}) M_{\odot} \text{ yr}^{-1}$ , in general agreement with results from recent hydrodynamical simulations. The dense knots have slow optical proper motions as well as relatively small X-ray-measured ionization timescales, which indicates that they were located a few pc away from the progenitor system and were only recently heated by forward shocks. Therefore, we argue that Kepler’s SN was an overluminous (91T-like) event that started to interact with massive CSM a few hundred years after the explosion. This supports the possible link between 91T-like SNe and the so-called “Ia-CSM” SNe — a rare class of SNe Ia associated with massive CSM. The link implies that  $\sim 10\%$  of SNe Ia are associated with massive CSM which most likely originates from a companion star in a single degenerate progenitor system.

*Subject headings:* ISM: individual objects (Kepler’s SNR, Tycho’s SNR, SNR 0509-67.5) — ISM: supernova remnants — circumstellar medium — supernovae: general — X-rays: general

## 1. Introduction

Type Ia supernovae (SNe Ia) are important astrophysical objects, as they play a central role in measuring the accelerative expansion of the universe and are primary source of iron-group elements (IGE) in the universe. However, the progenitor system(s) and detailed explosion mechanism(s) have been a matter of considerable debate (e.g., Maoz et al. 2014, for a recent review). It has been believed that SNe Ia are runaway thermonuclear explosions of a C/O white dwarf (WD), as it approaches the Chandrasekhar mass ( $\sim 1.4 M_{\odot}$ ). There are mainly two long-standing competing scenarios for how a WD increases its mass: (1) the single-degenerate model, in which a WD accretes material from a non-degenerate companion star in a close binary system (Whelan & Iben 1973); and (2) the double-degenerate model, in which two C/O WDs merge (Iben & Tutukov 1984; Webbink 1984). Therefore, identifying the progenitor stars (as a means of discriminating between the two scenarios) is an area of considerable activity in SN Ia studies.

There are many observational approaches to identifying progenitors, including studies

of potential progenitor populations (Hachisu & Kato 2001), searches for companions to the progenitor systems in optical pre/post-explosion images (e.g., Li et al. 2011b; Foley et al. 2014; McCully et al. 2014) and surviving companions in nearby supernova remnants (SNRs) (e.g., Schaefer & Pagnotta 2012; Bedin et al. 2014), and evidence of interactions between the SN ejecta and the companion star (e.g., Maeda et al. 2014). In addition, recent detection of a circumstellar medium in some SNe Ia (CSM: environmental gas modified by the mass loss from the progenitor systems) have opened a new window to infer progenitor systems.

The presence of a H-rich CSM itself supports the SD scenario, since such a CSM is not generally expected around two WDs in the DD scenario. Analysis of the CSM signature (both absorption and emission) offers further insight into the progenitor system. For example, time-variable Na I D absorption features, which were found in the normal Type Ia SN 2006X and a few others (Patat et al. 2007; Blondin et al. 2009; Simon et al. 2009), could be interpreted to arise from expanding shells (or knots) due to successive nova eruptions of the progenitor (Patat et al. 2007). Later, Sternberg et al. (2011) found that about half of all sampled SNe Ia (12/22) in their sample show blueshifted Na I D absorption lines, while only a quarter of them (5/22) show redshifted absorption, and the remaining quarter (5/22) show single or symmetric absorption profiles. They suggested that the biased detection of the blueshifted systems means a large fraction of SNe Ia ( $\gtrsim 25\%$ ) are associated with progenitors’ gas outflows (otherwise, we would see the same fractions of blueshifted and redshifted profiles). From the absorption column densities ( $N_{\text{NaI}} \sim 10^{12} \text{ cm}^{-2}$ ), the masses of the CSM shells have been estimated to be  $\lesssim 0.01 M_{\odot}$  (Patat et al. 2007), which are consistent with successive recurrent nova eruptions that swept up the stellar wind of the companion. Therefore, these CSM properties can be best explained by a symbiotic recurrent nova progenitor, similar to RS Ophiuchi.

Evidence for much more massive CSM ( $\sim 0.01\text{--}5 M_{\odot}$ ) has been found in several SNe Ia (SN 2002ic, SN 2005gj, SN 1997cy, SN 1999E, SN 2008J, PTF11kx, and some other candidates: Hamuy et al. 2003; Silverman et al. 2013, references therein). These SNe are called “SNe Ia-CSM” which are characterized by a narrow  $\text{H}\alpha$  line on top of an overluminous (SN 1991T-like or 91T-like) Ia template in the optical spectra. SNe Ia-CSM comprise only a small fraction of SNe Ia: 0.1–1 % (Dilday et al. 2012), albeit a true fraction may be somewhat larger, given a possibly significant amount of SNe Ia-CSM that are incorrectly classified as Type IIIn because of their spectral resemblance (Leloudas et al. 2013). While there are several proposed progenitor systems for Ia-CSM objects, none of them is yet conclusive.

Kepler’s SNR, the remains of SN 1604 A.D., is one of a handful of SNRs which are associated with historical Galactic SNe. Located at only 3–7 kpc (Kerzendorf et al. 2014, references therein), this remnant provides a precious opportunity to study details of SN Ia explosions

and the progenitor system. It belongs to a rare class of Type Ia SNRs (Kinugasa & Tsunemi 1999; Reynolds et al. 2007) that exhibit emission from a CSM, evidenced by the extremely high ambient density ( $\sim 100 \text{ cm}^{-3}$ ) at  $\gtrsim 500 \text{ pc}$  out of the Galactic plane and a N overabundance (Blair et al. 1991; Gerardy & Fesen 2001). Optical monitoring of 50 long-lived CSM knots revealed that they are moving fairly slowly, with a space velocity of  $\sim 280 \text{ km s}^{-1}$  at a distance of  $4.5 \text{ kpc}$  (Bandiera & van den Bergh 1991); reminiscent of quasi-stationary flocculi in Cassiopeia A. The trace-back time was measured to be  $3.2 \pm 1.2 \times 10^4 \text{ yrs}$ , which should be taken as a lower limit, given possible acceleration by the SN forward shock.

Douvion et al. (2001) found infrared (IR) emission from warm dust. Since the IR intensity map is similar to the distribution of the dense optical CSM knots, the authors argued that the IR emission arises from dust in the shocked CSM. Blair et al. (2007) further supported this picture based on *Spitzer Space Telescope* observations, and estimated the total shocked CSM mass to be  $\sim 1 M_{\odot}$  from their relatively cursory analysis of X-ray data. In addition to the CSM knots, the presence of a diffuse CSM has been inferred using followup *Spitzer* observations by Williams et al. (2012). Their work indicates that the CSM dust consists of two components: lower-temperature ( $\sim 80\text{--}100 \text{ K}$ ) dust behind fast shocks ( $> 1000 \text{ km s}^{-1}$ ) and penetrating into the tenuous ambient medium produces the majority of the IR emission; higher-temperature ( $> 150 \text{ K}$ ) dust behind slower shocks (a few hundred  $\text{km s}^{-1}$ ) penetrating into high density material ( $n \sim 50\text{--}250 \text{ cm}^{-3}$ ) coincides with the optical dense knots.<sup>1</sup> The presence of a CSM is also supported from recent hydrodynamic simulations (Velazquez et al. 2006; Chiotellis et al. 2012; Toledo-Roy et al. 2014; Burkey et al. 2013), where a high mass-loss rate of  $\dot{M} \sim 10^{-5} M_{\odot} \text{ yr}^{-1}$ , suggestive of dense winds from an asymptotic giant branch (AGB) star, can reasonably explain the observed expansion index and the north-south asymmetric morphology of Kepler’s SNR.

X-rays arise predominantly from SN ejecta, which are not detected at either optical or IR wavelengths. The X-ray spectrum exhibits strong Fe L lines and weak O K lines. A multi-component non-equilibrium ionization modeling suggests a Type Ia SN rather than a core-collapse SN as its origin (Kinugasa & Tsunemi 1999, references therein for a history of X-ray observations). From deep *Chandra* observations, Reynolds et al. (2007) confirmed the high Fe/O ratio and found no evidence for a neutron star, further supporting the Type Ia origin. Patnaude et al. (2012) claimed that Kepler’s SN was likely to be a 91T-like event that produced  $\sim 1 M_{\odot}$  of  $^{56}\text{Ni}$ , by comparing the observed X-ray spectrum with simulated spectra based on their hydrodynamic modeling at 400 yrs after the explosion. More recently, Park et al. (2013) performed a deep *Suzaku* observation, and found a high Mn/Cr line in-

---

<sup>1</sup>We note that dust is mainly heated by collisions in shocked gases, and that the efficiency of collisional heating increases with the density of the shocked gas.

tensity ratio of  $\sim 0.6$ , leading them to suggest a supersolar metallicity ( $\sim 3$  times the solar value) of the progenitor star.

Here, we investigate X-ray spectra of Kepler’s SNR and two other young Ia SNRs, Tycho’s SNR and SNR 0509-67.5, for comparison, by making the best use of available data from currently operational X-ray observatories. In the following section 2, we summarize the observations used. In sections 3 and 4, we perform X-ray spectral analyses, focusing mainly on the SN ejecta and the CSM, respectively. Finally, we discuss the observational results and lead to conclusions.

## 2. Observations and Data Reduction

We use archival data obtained by *XMM-Newton*, *Chandra*, and *Suzaku*, as summarized in Table 1. While our object of interest is Kepler’s SNR, we also analyze two similarly-aged Ia remnants, Tycho’s SNR and SNR 0509-67.5 in the Large Magellanic Cloud (LMC). Detailed classifications have already been determined for these two remnants, based on their light-echo spectra: Tycho is thought to be a prototypical Type Ia (Krause et al. 2008), SNR 0509-67.5 is thought to be “SN 1991T-like” (Rest et al. 2005). Thus these two remnants can serve as ideal reference targets to study the amount of IGE in Kepler’s SN.

We reprocessed the raw data, using version 13.5.0 of *XMM-Newton* Science Analysis Software, version 4.6 of *Chandra* Interactive Analysis of Observations, and version 22 of the *Suzaku* software, together with the latest versions of the calibration files at the analysis phase. For the X-ray Imaging Spectrometer (XIS: Koyama et al. 2007) onboard *Suzaku*, we focus on front-illuminated CCDs (XIS0 and XIS3) which have slightly better spectral resolution than the back-illuminated CCD (XIS1). We generated response files for the *XMM-Newton* Reflection Grating Spectrometer (RGS: den Herder et al. 2001), taking account of energy-dependent spatial structures in the source, as we did in our previous analyses of the Galactic SNR Puppis A (Katsuda et al. 2012, 2013). The first-order RGS spectral resolution, which is determined by the size of the remnants in our case, is roughly  $E/\Delta E \sim 25$  and 180 for Kepler’s SNR and SNR 0509-67.5, respectively. This resolution is higher than that of the XIS of  $E/\Delta E \sim 15$ .

Backgrounds (BGs) were taken from source-free regions in the same fields of view. The exception is the RGS spectrum for Kepler’s SNR, for which the spatial extent of the source-free areas is limited; hence we used blank-sky data (Obs. ID: 0051940401) taken immediately after the observation of Kepler’s SNR. Each spectrum was grouped into bins with at least 20 counts in order to allow us to perform a  $\chi^2$  test.

### 3. Ejecta Masses from Integrated X-Ray Spectra

#### 3.1. Glancing at *Suzaku*'s XIS Spectra of the Three SNRs

We first examine the wide-band X-ray spectra for the three SNRs. Figure 1 shows integrated *Suzaku* XIS spectra of the SNRs, where the intensities are normalized to equalize the Si He $\alpha$  line. A number of emission lines are apparent, mostly arising from the shocked SN ejecta. Obviously, the strengths of Fe lines (both L- and K-shell transitions) are quite different among the three sources, whereas K-shell lines from intermediate mass elements (IME: Si, S, Ar, and Ca) are similar to one another, in the sense that shock-heated IGE-to-IME mass ratios for Kepler's SNR and SNR 0509-67.5 are significantly larger than that for Tycho's SNR. It is reasonable to consider that the amount of unshocked cold ejecta in the three SNRs is similar among the remnants, based on their similar ages ( $\sim 400$  yr), close evolutionary states (Dickel et al. 1988; Reynoso et al. 1997; Katsuda et al. 2008; Vink 2008; Katsuda et al. 2010), and the similar reverse shock positions ( $\sim 70\%$  of the forward shock radius) as we describe below. Therefore, Kepler's SN must have produced a relatively large mass of IGE, similar to SNR 0509-67.5. When combined with information from light-echo spectra, i.e., overluminous for SNR 0509-67.5 and normal for Tycho's SNR, we argue that Kepler's SN was likely an overluminous Ia event.

This argument will be substantiated by our spectral fitting in the following section. There are reasons why spectral fitting is required to estimate the ejecta masses quantitatively and correctly. For example, while SNR 0509-67.5 has the strongest apparent Fe L lines below 1 keV in the raw XIS spectra in Fig. 1, these lines are considerably weaker than those of Kepler's SNR, if we correct for the interstellar absorption. Also notable is the slight shift of the line center energies of SNR 0509-67.5 with respect to those of the two Galactic SNRs. This shift is due not to artificial/instrumental effects, but to a mixture of bulk motions and ionization effects, as we will show below. Since the ionization state is sensitive to X-ray line intensities, we need to care about it in estimating ejecta masses. All of these effects can be accounted for through spectral fitting.

#### 3.2. Quantitative Mass Estimates Based on Spectral Fitting

In our spectral fitting, we use *XMM-Newton*'s RGS below 2 keV and *Suzaku*'s XIS above 2 keV for Kepler's SNR and SNR 0509-67.5. On the other hand, for Tycho's SNR, we use only data from *Suzaku*'s XIS, since the "slitless" RGS cannot provide a high-resolution spectrum due to the relatively large angular size of the remnant (diameter of  $\sim 8.5'$ ). Spatially-integrated X-ray spectra for the three SNRs are shown in Fig. 2. In these plots, only the

first-order RGS spectra are shown, but we use both first and second orders when modeling the data. The data points in blue for Kepler’s SNR is a local-BG subtracted CSM spectrum extracted from the summed-up regions of knots 1 and 2 (see, Section 4), by using *Chandra*’s Advanced CCD Imaging Spectrometer (ACIS: Garmire et al. 2003). We fit this spectrum with a CSM-only model having all normalizations of ejecta components fixed to zero, so that we can separate out the CSM emission as cleanly as possible. Note that, for the spectrum of Tycho’s SNR, we exclude data below 0.6 keV owing to poor signal-to-noise ratios due to a relatively heavy interstellar absorption together with the low energy tail emission from higher energy lines (Koyama et al. 2007), and in the 1.55 keV–1.75 keV band due to a Si-edge calibration concern with the XIS<sup>2</sup>.

We fit these spatially-integrated spectra with an absorbed, `vpshock` + three `vnei` + `power-law` + several Gaussian components model in the XSPEC package (Arnaud 1996). Here, the `vpshock` and the `power-law` components are supposed to be the thermal and synchrotron radiation, respectively, from the swept-up medium. The three `vnei` components represent emission from SN ejecta. At least three `vnei` components are required from a statistical point of view (F-test probability of >99%); we chose to not add more in order to keep our model as simple as possible. The several Gaussian components represent lines of Fe L and/or O K, Fe L and/or Ne K, Cr K, and Mn K not well represented in the broad band models.

While details of our parameter treatment can be found in Table 2, we elaborate some of them below. We fix the abundance of either Si/H or Fe/H to be  $10^5$  times the solar value, assuming that the three `vnei` components are nearly pure metal plasmas. Most of the emission from IME is reproduced by two `vnei` components, for which the two-components nature may reflect a temperature/density gradient within the shocked ejecta; e.g., a hydrodynamical model of Type Ia SNR evolution in a uniform ambient density predicts a strong temperature decrease (as well as density increase) from the reverse shock to the contact discontinuity (Dwarkadas et al. 1998). For these components, we tie the metal abundances to each other except for Fe (and Ni). The remaining `vnei` component is introduced to reproduce most of the Fe K emission. We assume the Ni/Fe abundance ratio to be that expected in the classical deflagration model (W7: Nomoto et al. 1984); the assumed value of Ni/Fe abundance does not affect our spectral fitting, since Ni lines are not clearly detected in the spectra. In this Fe-rich component, we allow abundances of Ar and Ca to vary freely; otherwise we see significant residuals at low-energy sides of the K lines of these elements, especially for Tycho’s SNR. This would indicate that some Ar and Ca may be mixed into IGE-rich layers, although

---

<sup>2</sup><http://heasarc.gsfc.nasa.gov/docs/suzaku/analysis/sical.html>

we cannot rule out other possibilities, e.g., the presence of strongly redshifted components for these elements. In any case, the ejecta masses will not change dramatically, hence we here adopt the simplest solution in terms of the spectral modeling.

We fix the absorbing column densities at  $N_{\text{H}} = 6.4 \times 10^{21} \text{ cm}^{-2}$ ,  $1 \times 10^{22} \text{ cm}^{-2}$ , and  $6 \times 10^{20} \text{ cm}^{-2}$  adopting elemental abundances given by Wilms et al. (2000) for Kepler’s SNR, Tycho’s SNR, and SNR 0509-67.5, respectively. The values for the two Galactic SNRs are determined by fitting synchrotron-dominated spectra from the outermost thin rims obtained by the *Chandra*’s ACIS, while that for SNR 0509-67.5 is taken from the literature (e.g., Warren et al. 2004; Williams et al. 2011). Free parameters are the electron temperature,  $kT_e$ , the ionization timescale,  $n_e t$ , the normalization defined as  $\int n_e n_{\text{H}} dV$  where  $n_e$  and  $n_{\text{H}}$  are electron and hydrogen densities and  $V$  is the emitting volume, and the redshift of each component, some of which are linked among different components in order to better constrain the parameters. Photon indices are allowed to vary freely. In addition, we multiply the `gsmooth` model to each thermal component in order to take account of line-broadening effects, for which we assume the widths to be proportional to the line energies.

As shown in Fig. 2, the best-fit models in green represent the data well. Individual components are shown in blue (swept-up medium), red (ejecta1 = the lower-temperature IME-dominated component), orange (ejecta2 = the higher temperature IME-dominated component), light blue (ejecta3 = the Fe-rich component), gray (power-law), and dotted black (Gaussians). Note for Kepler’s SNR that the swept-up components seen for both *XMM-Newton*’s RGS and *Chandra*’s ACIS have the same intrinsic spectral shapes, but look different due to distinct spectral responses. The lower panels in Fig. 2 show residuals; the red points represent the RGS second order data that are not shown in the upper panels. The reduced- $\chi^2$  values summarized in Table 2 are 1.38 (SNR 0509-67.5), 1.45 (Kepler’s SNR), and 2.91 (Tycho’s SNR). The relatively large value for Tycho’s SNR is not surprising, given that it is the brightest source of the three SNRs and the larger spectral bin widths (3.65 eV at the minimum using the XIS) than those of the other two sources ( $<1$  eV using RGS), making systematic uncertainties relatively serious for this SNR. We do not, however, introduce systematic uncertainties in our spectral fitting, since they do not affect our main conclusions.

We check the robustness of our spectral analysis by comparing the best-fit parameters in Table 2 with previous measurements. First of all, the N abundance of the swept-up (`vpshock`) component in Kepler’s SNR is quantitatively consistent with previous optical measurements (Blair et al. 1991), showing that this component is the CNO-processed stellar wind material, i.e., the CSM, as we expected. Also, the lines in the CSM component (mainly N Ly $\alpha$ , O He $\alpha$ , and O Ly $\alpha$ ) are significantly narrower than those of ejecta components, assuring robustness of the spectral separation between the CSM and the ejecta. Unfortunately, the data do

not allow us to measure N abundances or line widths of the CSM components for the other two SNRs because of the relatively poor spectral resolution (Tycho’s SNR) and statistics (SNR 0509-67.5). As for the photon indices, the best-fit values agree with previous X-ray measurements (e.g., Tamagawa et al. 2009; Cassam-Chenaï et al. 2007; Warren et al. 2004; Kosenko et al. 2008). In addition, by converting the line broadening of the ejecta component to bulk velocities, we obtain  $v_\sigma = 2740_{-60}^{+40} \text{ km s}^{-1}$ ,  $2970_{-10}^{+20} \text{ km s}^{-1}$ , and  $3570_{-230}^{+200} \text{ km s}^{-1}$  for Kepler’s SNR, Tycho’s SNR, and SNR 0509-67.5, respectively, where the velocities include effects of both thermal broadening and shell expansion whose contributions are hard to distinguish from our data. These are somewhat smaller than previous estimates for Tycho’s SNR (Hayato et al. 2010) and SNR 0509-67.5 (Kosenko et al. 2008), which might be explained by multiple ionization effects in our analysis.

We next look into details of ejecta components. Figure 3 illustrates unabsorbed spectra of the total ejecta components with intensities normalized at Si K-shell lines, in order to clearly reveal the differences among the three SNRs. We can readily see that the Fe K and L lines for Kepler’s SNR and SNR 0509-67.5 are much stronger than those for Tycho’s SNR. This is also evident from the spectral ratios in the lower panel. We then quantitatively estimate ejecta masses, using the best-fit parameters listed in Table 2. As the first step, we calculate  $n_e/n_H$  for each component, taking account of the elemental abundances and the ionization balance (in the SPEX code: Kaastra, et al. 1996) at the  $kT_e$  and  $n_e t$  values measured. With this information, we can calculate  $\int n_H^2 dV$  which can be converted to  $\int n_X^2 dV$  by multiplying each elemental abundance.

To deduce densities (and masses) from  $\int n_X^2 dV$ , we need to know emitting volumes of individual components. To this end, we generate deprojected radial profiles from high-angular resolution data obtained with the *Chandra*’s ACIS. We first extract energy-band images for 0.7–0.85 keV (Fe L), 0.9–1.2 keV (Fe L), 1.65–2.0 keV (Si K), 2.25–2.6 keV (S K), 2.95–3.25 keV (Ar K), 3.65–4.1 keV (Ca K), 4.0–6.0 keV (continuum), and 6.1–6.8 keV (Fe K). For each band image, we subtract continuum emission extrapolated according to the power-law slopes given in Table 2. We then generate continuum-subtracted radial profiles, by focusing on a smooth limb-brightened region of each SNR, i.e., north, west, and north-east for Kepler’s SNR, Tycho’s SNR, and SNR 0509-67.5, respectively, as shown in Fig. 4 upper panels. The radial profiles produced in this way for four selected energy bands are displayed in the middle panels of Fig. 4. We see a general trend, with Fe K, Fe L, and Si K peaking at increasing radius, consistent with a previous *XMM-Newton* study for Kepler’s SNR (Cassam-Chenaï et al. 2004). In addition, we find that the peak position of Ne-like Fe L lines (0.7–0.85 keV) is located systematically inside that of the more ionized Fe L lines (0.9–1.2 keV). This fact suggests that in each remnant, the Fe is indeed primarily SN ejecta heated by a reverse shock propagating toward the center. These radial profiles are depro-

jected by using the “onion-peeling” method, which estimates the emission at each radius repeated removal of the contribution from concentric outer shells (e.g., Fabian et al. 1980). The deprojected profiles are displayed in the lower panels in Fig. 4, where we do not give error bars as they strongly depend on the geometry of the ejecta, but the values should be  $\lesssim \pm 10\%$  if the assumed spherical symmetric distribution of the ejecta is correct.

These deprojected profiles are used to estimate emitting volumes of the individual `vnei` components. Since the profiles of Kepler’s SNR look similar to those of SNR 0509-67.5, we assume that the emitting geometries are the same. The reverse shock radii,  $R_{\text{RS}}$ , are taken to be the sharp rises of the Fe K (and Ne-like Fe L), which are 0.7 and 0.65 times the forward shock radii,  $R_{\text{FS}}$ , for Kepler’s SNR and Tycho’s SNR, respectively, where we define  $R_{\text{FS}}$  from eye inspections to be  $107''$ ,  $256''$ , and  $14.8''$  for Kepler’s SNR, Tycho’s SNR, and SNR 0509-67.5, respectively. We note that the value of  $R_{\text{RS}}$  found in this way for Tycho’s SNR is between those from a previous *Chandra* study (Warren et al. 2005) and a recent measurement from Fe  $K\beta$ ’s radial profiles with *Suzaku* (Yamaguchi et al. 2014). The hot, low-ionization, Fe-rich plasma (ejecta 3 in Table 2) resides in a layer from  $R_{\text{RS}}$  to  $0.85$  ( $0.75$ )  $R_{\text{FS}}$ , i.e., the inner radius of the half maximum of Si K’s deprojected profiles for Kepler’s SNR (Tycho’s SNR). Other IME-rich components, i.e., ejecta2 and ejecta3 in Table 2), occupy a shell outside the inner Fe-rich layers. The outer extent of the IME-rich components for Kepler’s SNR (Tycho’s SNR) is taken to be  $0.97$  ( $0.93$ )  $R_{\text{FS}}$ , which corresponds to the position where we see a sharp rise of the deprojected Si K profile for Kepler’s SNR (Tycho’s SNR). We note that the value for Tycho’s SNR represents the contact discontinuity suggested from a previous *Chandra* study (Warren et al. 2005). We allocate volume filling factors for the two IME-rich `vnei` components, such that their electron pressures are equalized:  $(f_{\text{ej1}} : f_{\text{ej2}}) = (0.05 : 0.95)$ ,  $(0.2 : 0.8)$ , and  $(0.015 : 0.985)$  for Kepler’s SNR, Tycho’s SNR, and SNR 0509-67.5, respectively. We then compute densities and masses for individual elements in each ejecta component.

We note that the surface brightness of Kepler’s SNR is quite asymmetric; the northern rim is much brighter than the southern rim. This could lead to biased mass estimates, if we use only one side (either north or south) of the rim in estimating emitting volumes. Therefore, we examine radial profiles of the southern portion in addition to those of the northern portion, finding that the reverse shock position as well as the IGE and IME layers are close to those of Tycho’s SNR rather than the northern portion of Kepler’s SNR. However, this modified emitting volumes result in only  $\sim 10\%$  variations of ejecta masses toward increasing/decreasing direction for IGE/IME. Such slight differences will not change our conclusion given below.

The estimates of integrated masses for the three ejecta components are summarized

in Table 3. We find that IGE masses for SNR 0509-67.5 and Kepler’s SNR are close to each other, but are higher than that for Tycho’s SNR. This result quantitatively confirms our expectation (from the spectral comparison in Figs. 1 and 3) that Kepler’s SN was an overluminous (91T-like) Ia event. This is also consistent with the result drawn by hydrodynamical modeling of the X-ray spectrum (Patnaude et al. 2012). A more convincing plot can be found in Fig. 6, in which we plot our data points on the IGE–IME mass diagram of 23 extragalactic SNe Ia (Mazzali et al. 2007) as in Fig. 6, where several 91T-like SNe are clustered in the upper left corner, a few subluminous (or 91bg-like) objects are distributed in the lower right corner, and many normal Ia objects are located in between them. We can see that Kepler’s SNR is well within the overluminous (91T-like) category, while Tycho’s SNR is among the normal SNe Ia. In this plot, SNR 0509-67.5 can be found in a marginal region between overluminous and normal Ia events. Therefore, this plot shows that the amount of IGE of Kepler’s SNR is even larger than that of the confirmed overluminous Ia SNR 0509-67.5, strongly supporting the idea that Kepler’s SN was an overluminous Ia event.

It should be noted in Table 3 that (1) we provide fairly conservative uncertainties which are much larger than those from the statistical uncertainties in Table 2; (2) we list unshocked IGE masses, based on SN Ia nucleosynthesis models (Nomoto et al. 1984; Maeda et al. 2010) combined with the reverse-shock positions estimated above; and (3) we assume that the total IME + IGE mass becomes  $\sim 1.05 M_{\odot}$  (Mazzali et al. 2007) by adjusting the distances to the remnants. The details are described below.

To evaluate the errors, we consider a wider range of the electron temperature for the hot Fe-rich component than the statistical uncertainties, given possible systematic uncertainties on Fe L emissivities. In fact, even if we fix  $kT_e = 2 \text{ keV}$  and  $kT_e = 15 \text{ keV}$  for this component, we derive similar quality fits; reduced- $\chi^2$  values for  $kT_e = 2 \text{ keV}$  and  $15 \text{ keV}$  are, respectively, 1.54 and 1.49 for Kepler’s SNR, 3.55 and 3.02 for Tycho’s SNR, and 1.42 (for both 2 keV and 15 keV) for SNR 0509-67.5. Thus, we consider these extreme temperature cases to be viable, and they provide the major source of the large uncertainties in Table 3.

The upper two rows of Figure 5 show the masses of shocked IME and IGE as a function of distance for three cases: the best fits in the red solid curves;  $kT_e = 2 \text{ keV}$  in the black dashed curves; and  $kT_e = 15 \text{ keV}$  in the black dotted curves. The third row shows unshocked ejecta masses for two SN Ia abundance distributions: the classical W7 model (the upper curve: Nomoto et al. 1984) and a two-dimensional (azimuthally-averaged) delayed-detonation model, i.e., off-center ignition O-DDT model (the lower curve: Maeda et al. 2010). While both of the two models are not responsible for overluminous Ia SNe but for normal Ia SNe, the amount and composition of the unshocked ejecta would not be different by much, since the abundance distributions of the two models examined here look (more) similar to

those of overluminous cases rather than subluminous cases by Seitenzahl et al. (2013). To estimate the cold ejecta masses, we integrate the ejecta masses from  $v_{\text{ej}} = 0$  up to  $v_{\text{ej}} = R_{\text{rs}}/\text{age}$  (the free expansion velocity at the reverse shock). We find that the composition of the unshocked ejecta is almost pure IGE for both models, hence we name the y-axis label as “cold IGE.” The bottom panels show the total masses (hot IME + hot IGE + cold IGE).

In principle, the ejecta masses can take any values (even unrealistic ones), by changing the temperature and/or distances (see Fig. 5). Therefore, we introduce one constraint that the total masses of IGE plus IME are within  $0.96\text{--}1.14 M_{\odot}$ , according to a systematic analysis of 23 samples of well-observed extragalactic SNe Ia (Mazzali et al. 2007). In the bottom panels, this mass range is given as horizontal dotted lines. Limiting the total masses in this range, we can constrain distances to the remnants for each temperature case. The distances for the best-fit cases (in between the two solid red lines) are  $\sim 4.2$  kpc,  $\sim 2.55$  kpc, and  $\sim 46$  kpc for Kepler’s SNR, Tycho’s SNR, and SNR 0509-67.5, respectively. While the values for the two Galactic SNRs agree with some of previous estimates (Sankrit et al. 2005; Katsuda et al. 2008; Vink 2008; Chevalier et al. 1980; Albinson et al. 1986), all of the distances are slightly smaller than the canonical values (Kerzendorf et al. 2014; Hayato et al. 2010; Alves 2004; Macri et al. 2006). In particular, the distance to SNR 0509-67.5 in the LMC is relatively well determined. Thus, if we set the distance to the current best estimate of 48.1 kpc (Macri et al. 2006), we obtain the total IME+IGE mass to be  $\sim 1.2 M_{\odot}$  (see, Fig. 5). This is just slightly larger than the upper end ( $1.14 M_{\odot}$ ) expected for SNe Ia (Mazzali et al. 2007), and such a deviation would be still acceptable. On the other hand, there is also a possibility that SNR 0509-67.5 whose absorption within the LMC is negligible is indeed located at  $\sim 2$  kpc front side with respect to the main body of the LMC. Since accurate measurements of the total masses and distances, which require significant additional analysis efforts, are beyond the scope of this paper, we leave this issue for future work based on high-resolution X-ray spectra which will be available with the upcoming *ASTRO-H* (Takahashi et al. 2014). Keeping the total IME+IGE masses within  $0.96\text{--}1.14 M_{\odot}$ , we calculate allowed masses of the IME and IGE for the three temperature cases ( $kT_{\text{e}} = 2$  keV, 15 keV, and the best-fit). The resultant nominal values along with the uncertainties are given in Table 3.

#### 4. The Circumstellar Medium in Kepler’s SNR

We perform spatially-resolved spectral analyses to reveal details of the CSM, using the *XMM-Newton* RGS as well as the *Chandra* ACIS. Our particular interest is to search for X-ray emission from the “diffuse” CSM found by Williams et al. (2012) using *Spitzer* IR observations in the form of a lower temperature dust component, distinct from the hotter dust

component associated with dense/knotty CSM. To this end, we extract an RGS spectrum from the region within the solid lines in Fig. 7, where no CSM knots are present. Figure 8 displays the RGS spectrum together with the best-fit model — the same model as we applied to the integrated spectra in Fig. 2. We find a line feature at  $\sim 0.5$  keV, which can be modeled by N Ly $\alpha$  arising from the swept-up component. The best-fit parameters are listed in Table 2; they show the presence of an enhanced N abundance in the swept-up component, similar to that found for the entire remnant (Figure 2 and Table 2). This is evidence that this component originates from the CNO-processed CSM, revealing that the diffuse CSM can be seen in X-rays as well as in the IR (Williams et al. 2012).

The diffuse CSM can be reasonably interpreted as material in steady outflow from the progenitor system, which refilled a cavity created by the major eruption a few  $10^4$  yrs ago suggested by optical proper motions of the CSM knots (Bandiera & van den Bergh 1991). The density and the mass of the diffuse CSM are calculated to be  $2.8 \text{ cm}^{-3}$  and  $0.08 M_{\odot}$ , respectively, at a distance of 4.2 kpc, based on the assumption that the emitting region is a polar-cap shell of  $0.97\text{--}1 R_{\text{FS}}$  with a filling factor of unity. This density is consistent with that inferred from IR observations (Williams et al. 2012). The total mass integrated over the entire remnant is  $\sim 0.3 M_{\odot}$ , given that the region we examined covers only  $\sim 30\%$  of the entire remnant. It should be noted that the total mass might increase by a factor of a few if we take into account the north-south asymmetry seen in both the IR and X-rays. Assuming a wind speed of  $v_w = 10 \text{ km s}^{-1}$ , we estimate a mass-loss rate of  $1.5 \times 10^{-5} (v_w / 10 \text{ km s}^{-1}) M_{\odot} \text{ yr}^{-1}$ , is needed to provide the estimated mass of  $0.3 M_{\odot}$  within a radius of 2.1 pc at a distance of 4.2 kpc. Such a large mass-loss rate suggests that the progenitor is an AGB star, which is consistent with results from recent hydrodynamical simulations (Velazquez et al. 2006; Chiotellis et al. 2012; Toledo-Roy et al. 2014).

Next, we turn to the bright knotty features which are positionally coincident with optically bright knots. We examine five such features (Knots 1–5) as shown in Fig. 7. By subtracting local BGs (dashed regions next to the source regions), we extract clean CSM spectra. The spectra are fitted by a single-component `vpshock` model. In the fitting procedure, the  $kT_e$ ,  $n_e t$ , and normalization are treated as free parameters. Abundances of O, Ne, and Mg are allowed to vary freely for the brightest Knots 1 and 2, while we fix all metal abundances to the solar values for the other relatively-dim knots. The spectra with the best-fit models are shown in Fig. 9. The best-fit parameters are summarized in Table 4. The temperatures and ionization timescales are roughly consistent with those derived from the integrated RGS spectrum (Table 2) and previous *Chandra* measurements (Reynolds et al. 2007).

To derive densities and masses, we assume the X-ray-emitting plasma’s geometry to be

spherical for Knot-2 and a rugby-ball shape for the others. We also assume filling factors to be unity for all the regions. The estimated densities and masses are listed in Table 4. The densities are an order of magnitude lower than the optical measurements (Dennefeld 1982), suggesting that X-rays arise from relatively tenuous regions surrounding (or close to) optical dense cores. The total mass of the five regions is  $1.1 \times 10^{-3} M_{\odot}$ . Clearly, these regions contain quite limited amounts of the total CSM knots, since the optical CSM knots are distributed more widely than the selected regions (e.g., Bandiera & van den Bergh 1991). Indeed, the normalization summed-up for the five regions (see, Table 4) is only  $\sim 1/40$  of the RGS-measured normalization integrated for the entire remnant (see, Table 2). Part of the integrated normalization should be attributed to the diffuse CSM, whose fraction is estimated to be  $\sim 20\%$ , based on the normalizations of the entire remnant and the southern part in Table 2. Thus, we infer the total mass of the knotty CSM in the entire remnant to be  $\sim 0.035 M_{\odot}$  ( $= 1.1 \times 10^{-3} M_{\odot} \times 40 \times 0.8$ ). This would be slightly increased by adding optically emitting knots. Such a large amount of the CSM is consistent with those observed in SNe Ia-CSM.

Unlike Ia-CSM SNe, the dense/knotty CSM in Kepler’s SNR is located far away from the progenitor star, as evidenced by three independent pieces of information. First, the slow proper motions of the CSM knots measured in optical (Bandiera & van den Bergh 1991) allow movements of only  $5.3''$  (or  $0.1$  pc at a distance of  $4.2$  kpc) after the explosion. This is evidence that the knots were already  $\sim 2$  pc (i.e., the SNR radius) away from the progenitor star at the time of the SN explosion. Second, dividing the ionization timescale by the electron density in Table 4, we infer the shock-heating time to be  $\sim 50$ – $200$  yrs. This means that interactions between the CSM and the blastwave started at a very late phase, i.e.,  $\gtrsim 200$  yrs after the explosion. Third, the light curve of Kepler’s SN does not show any hints of early-phase CSM interactions. Figure 10 shows two light curves of Kepler’s SN obtained by European observers in black and Korean observers in red (Baade 1943; Clark & Stephenson 1977; Schaefer 1996). For comparison, we show typical light curves of several kinds of SNe, i.e., Ia-CSM (SN 2002ic: Wood-vasey et al. 2004), 91T-like (SN 1991T: Lira et al. 1998), 91bg-like (SN 1991bg: Filippenko et al. 1992), and Type IIp (SN 1999em: Elmhamdi et al. 2003). All of the light curves are normalized such that their peak magnitude is zero, in order to highlight the difference of their shapes. We find that the light curves of Kepler’s SN (both European and Korean versions) are clearly distinct from that of SN 2002ic (Ia-CSM), showing that there was no massive CSM in close proximity to the progenitor ( $\lesssim 0.01$  pc). This assertion would be fairly robust, given that both of the two independent historical light curves, generally agreeing with each other within 1 mag, decline quite fast ( $\Delta \text{mag} \sim 5$  at  $\text{day} \sim 100$  from the maximum light), which is in stark contrast to the flat light curves seen for SNe Ia-CSM.

## 5. Discussion

Our work strongly suggests that Kepler’s SN was likely to be a 91T-like event, based on the ejecta abundances — the dominance of IGE. Since detailed light curves of Kepler’s SN were taken by both European and Korean observers in A.D.1604–1605, it is interesting to ask if these light curves are consistent with those of overluminous SNe Ia obtained by modern telescopes. Unfortunately, we found it difficult to discriminate the overluminous and subluminoous SNe Ia from the light-curve shapes. As shown in Fig. 10, the light curve measured by Johannes Kepler and some other European is best represented by that of SN 1991T, whereas the Korean version (red data in Fig. 10) is closer to that of SN 1991bg (subluminous). This discrepancy probably means that brightness uncertainties from naked-eye measurements are too large to discriminate among SNe Ia subtypes that follow the light-curve decline rate versus peak luminosity correlation (i.e., the “Phillips relation”: Phillips 1999). Another important piece of information from the light curve is the peak brightness. Assuming the absolute maximum brightness of Kepler’s SN to be -19.5 mag, a typical value for 91T-like events, and a visual extinction to be 3.27 mag (Schaefer 1996), we estimate the distance to Kepler’s SNR to be either 6.3 kpc or 4.5 kpc from the apparent maximum brightness (-2.25 or -2.95) reported in Europe and Korea, respectively. Therefore, the apparent maximum brightness from the Korean observations matches our result better. We should, however, note that the distance of 6.3 kpc from European maximum brightness is more consistent with recently preferred value of  $\sim 6$  kpc. Given these considerations, the only solid conclusion from the light curve studies is that Kepler’s SN was different from Ia-CSM and Type IIp, but was close to Phillips-relation SNe Ia.

In addition, we confirmed the presence of dense X-ray emitting CSM in Kepler’s SNR, and estimated its total mass in the entire remnant to be  $\sim 0.035 M_{\odot}$ . This large mass reminds us of the massive CSM associated with SNe Ia-CSM. However, as we discussed above, the light curve is inconsistent with a Ia-CSM event for Kepler’s SN, suggesting the different distances between the CSM and the progenitor star; a few pc away from the progenitor for Kepler’s SN is much farther than those seen in Ia-CSM events ( $\lesssim 0.01$  pc). Thus, we argue that Kepler’s SN was likely to be a 91T-like event, and started to interact with the dense CSM  $\gtrsim 200$  yrs after the SN explosion.

In this way, Kepler’s SNR has provided us with observational evidence for a recently proposed connection between 91T-like events and Ia-CSM objects: i.e., the two Ia subclasses are actually the same phenomenon with seeming differences due to different timing of the interaction with a massive CSM (Leloudas et al. 2013). This speculation was originally inspired by optical observations of SN 2002ic and PTF11kx, whose optical spectra initially resembled a 91T-like template, but started to develop an H $\alpha$  line after 22 days and 59 days

after explosions, respectively, evolving to more like a Type IIn template. Since the timing of the CSM interaction is not unique, we can easily guess a possibility that the timing was too late to show signatures of the CSM, as the SNe fade after the explosions. While such SNe would be classified as 91T-like events, if we could monitor them for several hundred years, we should be able to detect a signature of a massive CSM. We believe that Kepler’s SN must be such an example, and speculate that another overluminous Ia remnant, SNR 0509-67.5, might show strong interaction with a massive CSM in the future. It should be noted that, whereas Ia-CSM objects occupy only 0.1–1% of SNe Ia (Dilday et al. 2012), the fraction of 91T-like events is  $\sim 9\%$  (Li et al. 2011a). Therefore, our result implies that roughly 10% of SNe Ia are associated with a massive CSM.

Based on the observational clues obtained so far, we discuss possible progenitor systems for Kepler’s SNR. First of all, the presence of the CSM itself favors the SD scenario. While some recent DD models predict the existence of CSMs (Shen et al. 2013; Raskin & Kasen 2013; Tanikawa et al. 2015), they originate from a H-rich envelope of a He WD or tidal tails from a C/O WD, hence they would not be CNO-processed N-rich material. This is in conflict with the overabundance of N seen in the CSM of Kepler’s SNR. Moreover, the small amount of O ejecta,  $< 0.069 M_{\odot}$  as shown in Table 3, is not expected for DD scenarios (e.g., Pakmor et al. 2011; Röpke et al. 2012), but is more consistent with delayed-detonation Chandrasekhar-mass models (e.g., Maeda et al. 2010; Seitenzahl et al. 2013). Therefore, there is no observational support for DD channels as the origin of Kepler’s SN, except for the absence of a candidate surviving companion star (Kerzendorf et al. 2014).

Outflows from SD progenitors can originate from either the exploding star or the donor star. For Kepler’s SN, the former case is less likely than the latter. This is because the exploding star, which must have experienced a major mass loss  $\sim 3 \times 10^4$  yrs before the explosion, cannot have had sufficient time to evolve to a WD and accrete material from its donor star to near the Chandrasekhar mass (cf., accretion timescale is of the order of  $10^6$  yrs). On the other hand, the exploding star is not necessarily a WD — the so-called Type 1.5 model predicts that a degenerate C/O core of a massive ABG star with very low metallicity grows to near the Chandrasekhar mass before it loses its envelope (Arnett 1969; Iben & Renzini 1983; Lau et al. 2008). However, such a SN occurs inside a massive H envelope, so that the SN light curve should look like Type Iip SNe as shown in Fig. 10 (K.Maeda et al. in preparation). Looking at Fig. 10, this is evidently not the case for Kepler’s SN. Moreover, the fact that the metallicity of Kepler’s CSM is nearly solar (Table 4) also conflicts with the Type 1.5 model.

Turning to outflows from a companion/donor star, the high mass-loss rate we estimated,  $\dot{M} \sim 1.5 \times 10^{-5} (v_w/10 \text{ km s}^{-1}) M_{\odot} \text{ yr}^{-1}$ , suggests an AGB companion. One possible progeni-

tor system hosting an AGB companion is a recurrent nova (Hachisu & Kato 2001). However, there are two major observational facts contrary to the recurrent novae scenario. First, Kepler’s SN experienced a major mass eruption  $\sim 3 \times 10^4$  yrs before the SN explosion. Such a long nova timescale is not expected for recurrent nova systems with near Chandrasekhar-mass WDs, for which typical recurrence times are 10–100 yrs. Second, according to numerical simulations (Marietta et al. 2000), the impact of SN ejecta removes most of the envelope of a companion star if it is a giant like an AGB star. As a result, the surviving companion will evolve away from the red giant branch, along a track of constant luminosity ( $\sim 10^3 L_\odot$ ) for at least  $10^5$  yrs. Such a bright star, if present, should be easily detected by optical observations, but is not detected at least near the center of the remnant (Kerzendorf et al. 2014). Thus, a recurrent nova is not likely the progenitor of Kepler’s SN, either.

There are other models that satisfy observational properties of Kepler’s SNR, i.e., both high mass-loss rate and no bright surviving companion. In efforts to explain the progenitor system of SNe Ia-CSM, Han & Podsiadlowski (2006) investigated the classical supersoft channel that consists of a C/O WD and a main sequence star. They found that if the donor star is a relatively massive ( $\sim 3 M_\odot$ ) main sequence star and the system experiences delayed dynamical instabilities, a large amount of mass can be lost from the system in the last few  $10^4$  yrs before the explosion. As a result, the donor star loses most of the mass before the explosion, and its luminosity becomes as low as the sun. This model can explain both the massive CSM and no detectable surviving companion in Kepler’s SNR. Alternatively, Soker et al. (2013) argued that a WD and a hot core of a massive AGB star in a common envelope will violently and promptly merge if the WD is denser than the core. In this case, there is no surviving companion left behind the SN while massive a CSM could be present near the progenitor system, making this model viable as well. However, we have not yet found observational evidence supporting these models, leaving us the mystery of the progenitor system. Continuous searches for a surviving companion and/or signatures of a companion star in Kepler’s SNR would be of great importance for revealing the progenitor of Kepler’s SNR and SNe Ia in general.

## 6. Conclusions

We have analyzed X-ray spectra and images of three young ( $\sim 400$  yrs old), ejecta-dominated SNRs, i.e., Kepler’s SNR, Tycho’s SNR, and SNR 0509-67.5 in the LMC. A simple spectral comparison among the three remnants suggests that Kepler’s SNR and SNR 0509-67.5 produced substantially more IGE than Tycho’s SNR. In fact, we quantitatively revealed that the IGE masses for both Kepler’s SNR and SNR 0509-67.5 are similar to those of

overluminous SNe Ia, while that for Tycho’s SNR is comparable to that of normal SNe Ia, assuming the total mass of IME and IGE to be  $\sim 1.05 M_{\odot}$  (Mazzali et al. 2007) and inferring the unshocked ejecta masses using the SN Ia’s nucleosynthetic models together with the reverse shock positions estimated from *Chandra* images. This inference is consistent with the fact that SNR 0509-67.5 and Tycho’s SNR are confirmed remnants of overluminous and normal SNe Ia explosions, respectively. Therefore, we conclude that Kepler’s SN was likely an overluminous (91T-like) event. Our method is quite simple, and thus could be a powerful tool for discriminating subclasses of Type Ia SNRs.

The *XMM-Newton*’s RGS spectrum shows a strong N Ly $\alpha$  line for Kepler’s SNR. We measured the N/H abundance to be  $\sim 4$  times the solar value, suggesting the presence of a CNO-processed CSM as was previously suggested by optical spectroscopy (Blair et al. 1991). We revealed that the CSM is comprised of diffuse gas and dense knots. The CSM masses are estimated to be  $\sim 0.3 M_{\odot}$  and  $\sim 0.035 M_{\odot}$  for the diffuse gas and dense knots, respectively. The mass of the diffuse CSM allows us to infer a mass-loss rate of the progenitor system to be  $\sim 1.5 \times 10^{-5} (v_w/10 \text{ km s}^{-1}) M_{\odot} \text{ yr}^{-1}$ , consistent with those of AGB stars. As for the knots, their slow optical proper motions and ionization timescales measured by using X-ray spectra suggest that they were located far away from the progenitor system at the time of SN explosion, and were recently shock heated. We argue that Kepler’s SN was likely a 91T-like event that started to interact with massive CSMs a few hundred years after the explosion. This supports the possible link between 91T-like SNe and SNe Ia-CSM, implying that  $\sim 10\%$  of SNe Ia are associated with massive CSM. All of these SNe would be related to a single degenerate channel.

This work is supported by Japan Society for the Promotion of Science KAKENHI Grant Numbers 25800119 (S.Katsuda), 24740167 (K.Mori), 23740141, 26800100 (K.Maeda), 24740117, 15H02075, 15H00788 (M.Tanaka), 24540229 (K.Koyama), 23000004 (H.Tsunemi), 26670560 (H.Nakajima), 25105516 (Y.Maeda), and 24654052 (M.Ozaki).

## REFERENCES

- Albinson, J.S., Tufts, R.J., Swinbank, E., & Gull, S.F. 1986, *MNRAS*, 219, 427
- Alves, D.R. 2004, *New Astronomy Reviews*, 48, 659
- Arnett, W.D. 1969, *Astrophysics and Space Science*, 5, 180
- Arnaud, K.A. 1996, in *ASP Conf. Ser. 101, Astronomical Data Analysis Software and Systems V* ed. G.H. Jacoby & J. Barnes (San Francisco: ASP), 17

- Baade, W. 1943, *ApJ*, 97, 119
- Badenes, C., Hughes, J.P., Bravo, E., & Langer, N. 2007, *ApJ*, 662, 472
- Bandiera, R., & van den Bergh, S. 1991, *ApJ*, 374, 186
- Bedin, L.R., Ruiz-Lapuente, P., Gonzalez Hernandez, J.I., Canal, R., Filippenko, A.V., & Mendez, J. 2014, *MNRAS*, 439, 354
- Blair, W.P., Long, K.S., & Vancura, O. 1991, *ApJ*, 366, 484
- Blair, W.P., Ghavamian, P., Long, K.S., Williams, B.J., Borkowski, K.J., Reynolds, S.P., & Sankrit, R. 2007, *ApJ*, 662, 998
- Blondin, S., Prieto, J.L., Patat, F., Challis, P., Hicken, M., Kirshner, R.P., Matheson, T., & Modjaz, M. 2009, *ApJ*, 693, 207
- Burkey, M.T., Reynolds, S.P., Borkowski, K.J., & Blondin, J.M. 2013, *ApJ*, 764, 63
- Cassam-Chenaï, G., Decourchelle, A., Ballet, J., Hwang, U., Hughes, J.P., & Petre, R. 2004, *A&A*, 414, 545
- Cassam-Chenaï, G., Hughes, J.P., Ballet, J., & Decourchelle, A. 2007, *ApJ*, 665, 315
- Chevalier, R.A., Kirshner, R.P., & Raymond, J.C. 1980, *ApJ*, 235, 186
- Chiotellis, A., Schure, K.M., & Vink, J. 2012, *A&A*, 537, 139
- Clark, D.H., & Stephenson, F.R. 1977, *The Historical Supernovae* (Oxford: Pergamon)
- den Herder, J. W., et al. 2001, *A&A*, 365, L7
- Dickel, J.R., Sault, R., Arendt, R.G., Korista, K.T., & Matsui, Y. 1988, *ApJ*, 330, 254
- Dilday, B., et al. 2012, *Science*, 2012, 337, 942
- Douvion, T., Lagage, P.O., Cesarsky, C.J., & Dwek, E. 2001, *A&A*, 373, 281
- Dwarkadas, V., & Chevalier, R.A. 1998, *ApJ*, 497, 807
- Elmhamdi, A., et al. 2003, *MNRAS*, 338, 939
- Fabian, A.C., Willingale, R., Pye, J.P., Murray, S.S., & Fabbiano, G. 1980, *MNRAS*, 193, 175
- Filippenko, A.V., et al. 1992, *ApJ*, 104, 1543

- Foley, R.J., McCully, C., Jha, S.W., Bildsten, L., Fong, W-F., Narayan, G., Rest, A., Stritzinger, M.D. 2014, ApJ, 792, 29
- Garmire, G.P., Bautz, M.W., Ford, P.G., Nousek, J.A., Ricker, G.R., Jr. 2003, SPIE,4851,28
- Gerardy, C.L., & Fesen, R.A. 2001, ApJ, 121, 2781
- Hachisu, I., & Kato, M. 2001, ApJ, 558, 323
- Han, Z., & Podsiadlowski, Ph. 2006, MNRAS, 368, 1095
- Hamuy, B., et al. 2003, Nature, 424, 651
- Hayato, A., et al. 2010, ApJ, 725, 894
- Iben, I., Jr., & Renzini, A. 1983, 21, 271
- Iben, I., Jr., & Tutukov, A.V. 1984, ApJS, 54, 335
- Kaastra, J. S., Mewe, R., Liedahl, D. A., Singh, K. P., White, N. E., & Drake, S. A. 1996, A&A, 314, 547
- Katsuda, S., Tsunemi, H., Uchida, H., & Kimura, M. 2008, ApJ, 689, 225
- Katsuda, S., Petre, R., Hughes, J.P., Hwang, U., Yamaguchi, H. Hayato, A., Mori, K., & Tsunemi, H. 2010, ApJ, 709, 1387
- Katsuda, S., et al. 2012, ApJ, 756, 49
- Katsuda, S., Ohira, Y., Mori, K., Tsunemi, H., Uchida, H., Koyama, K. & Tamagawa, T. 2013, ApJ, 768, 182
- Kerzendorf, W.E., Childress, M., Scharwächter, J. Do, T., & Schmidt, B.P. 2014, ApJ, 782, 27
- Kinugasa, K., & Tsunemi, H. 1999, PASJ, 51, 239
- Korn, A.J., Keller, S.C., Kaufer, A., Langer, N., Przybilla, N., Stahl, O., & Wolf, B. 2002, A&A, 385, 143
- Kosenko, D., Vink, J., Blinnikov, S., & Rasmussen, A. 2008, A&A, 490, 223
- Koyama, K., et al. 2007, PASJ, 59, S23
- Krause, O., Tanaka, M., Usuda, T., Hattori, T., Goto, M., Birkmann, S., & Nomoto, K. 2008, Nature, 456, 617

- Lau, H.H.B., Stancliffe, R.J., Tout, C.A. 2008, MNRAS, 301, 385
- Leloudas, G., et al. 2013, submitted to A&A (arXiv:1306.1549)
- Li, W., et al. 2011, MNRAS, 412, 1441
- Li, W., et al. 2011, Nature, 480, 348
- Lira, P., et al. 1998, ApJ, 115, 234
- Macri, L.M., Stanek, K.Z., Bersier, D., Greenhill, L.J., & Reid, M. J. 2006, ApJ, 652, 1133
- Maeda, K., Röpke, F.K., Fink, M., Hillebrandt, W., Travaglio, C. Thielemann, F.-K. 2010, ApJ, 712, 624
- Maeda, K., Kutsuna, M., & Shigeyama, T. 2014, ApJ, 794, 37
- Maoz, D., Mannucci, F., & Nelemans, G. 2014, Annual Review of Astronomy and Astrophysics, 52, 107
- Marietta, E., Burrows, A., & Fryxell, B. 2000, ApJS, 128, 615
- Mazzali, P.A., Röpke, F.K., Benetti, S., & Hillebrandt, W. 2007, Science, 315, 825
- McCully, C., et al. 2014, Nature, 512, 54
- Nomoto, K., Thielemann, F.-K., & Yokoi, K. 1984, ApJ, 286, 644
- Pakmor, R., Hachinger, S., Röpke, F.K., & Hillebrandt, W. 2011, A&A, 528, 117
- Park, S., et al. 2013, ApJL, 767, L10
- Patat, F., et al. 2007, Science, 317, 924
- Patnaude, D.J., Badenes, C., Park, S., & Laming, J.M. 2012, ApJ, 756, 6
- Phillips, M.M. Lira, P., Suntzeff, N.B., Schommer, R.A., Hamuy, M., Maza, J. 1999, AJ, 118, 1766
- Raskin, C., & Kasen, D. 2013, ApJ, 772, 1
- Rest, A., et al. 2005, Nature, 438, 1132
- Reynolds, S.P., Borkowski, K.J., Hwang, U., Hughes, J.P., Badenes, C., Laming, J.M., & Blondin, J.M. 2007, ApJ, 668, L135

- Reynoso, E.M., Moffett, D.A., Goss, W.M., Dubner, G.M., Dickel, J.R. Reynolds, S.P., & Giacani, E.B. 1997, *ApJ*, 491, 816
- Röpke, F.K., et al. 2012, *ApJL*, 750, L19
- Russell, S.C., & Dopita, M.A. 1992, *ApJ*, 384, 508
- Sankrit, R., Blair, W.P., DeLaney, T., Rudnick, L., Harrus, I.M., & Ennis, J.A. 2005, *Adv. Space Res.*, 35, 1027
- Schaefer, B.E. 1996, *ApJ*, 459, 438
- Schaefer, B.E. & Pagnotta, A. 2012, *Nature*, 481, 164
- Seitzzahl, I.R., et al. 2013, *MNRAS*, 429, 1156
- Shen, K.J., Guillochon, J., & Foley, R.J. 2013, *ApJL*, 770, L35
- Silverman, J.M., et al. 2013, *ApJS*, 207, 3
- Simon, J.D., et al. 2009, *ApJ*, 702, 1157
- Soker, N., Kashi, A., Garcia-Berro, E., Torres, S., & Camacho, J. 2013, *MNRAS*, 431, 1541
- Sternberg, A., et al. 2011, *Science*, 2011, 333, 856
- Takahashi, T., et al. 2014, *Proceedings of the SPIE*, 9144, 25
- Tamagawa, T., et al. 2009, *PASJ*, 61, S167
- Tanikawa, A., Nakasato, N., Sato, Y., Nomoto, K., Maeda, K., Hachisu, I. 2015, *ApJ*, in press
- Toledo-Roy, J.C., Esquivel, A., Velazquez, P.F., & Reynoso, E.M. 2014, *MNRAS*, 442, 229
- Dennefeld, M. 1982, *A&A*, 112, 215
- Velazquez, P.F., Vigh, C.D., Reynoso, E.M., Gomez, D.O., & Schneider, E.M. 2006, *ApJ*, 649, 779
- Vink, J. 2008, *ApJ*, 689, 231
- Warren, J.S., & Hughes, J.P. 2004, *ApJ*, 608, 261
- Warren, J.S., et al. 2005, *ApJ*, 634, 376

Webbink, R.F. 1984, ApJ, 277, 355

Whelan, J., & Iben, I., Jr. 1973, ApJ, 186, 1007

Williams, B.J., et al. 2011, ApJ, 729, 65

Williams, B.J., Borkowski, K.J., Reynolds, S.P., Ghavamian, P., Blair, W.P., Long, K.S., & Sankrit, R. 2012, ApJ, 755, 3

Wilms, J., Allen, A., & McCray, R. 2000, ApJ 542, 914

Wood-Vasey, W.M., Wang, L., & Aldering, G. 2004, ApJ, 616, 339

Yamaguchi, H., et al. 2014, ApJ, 780, 136

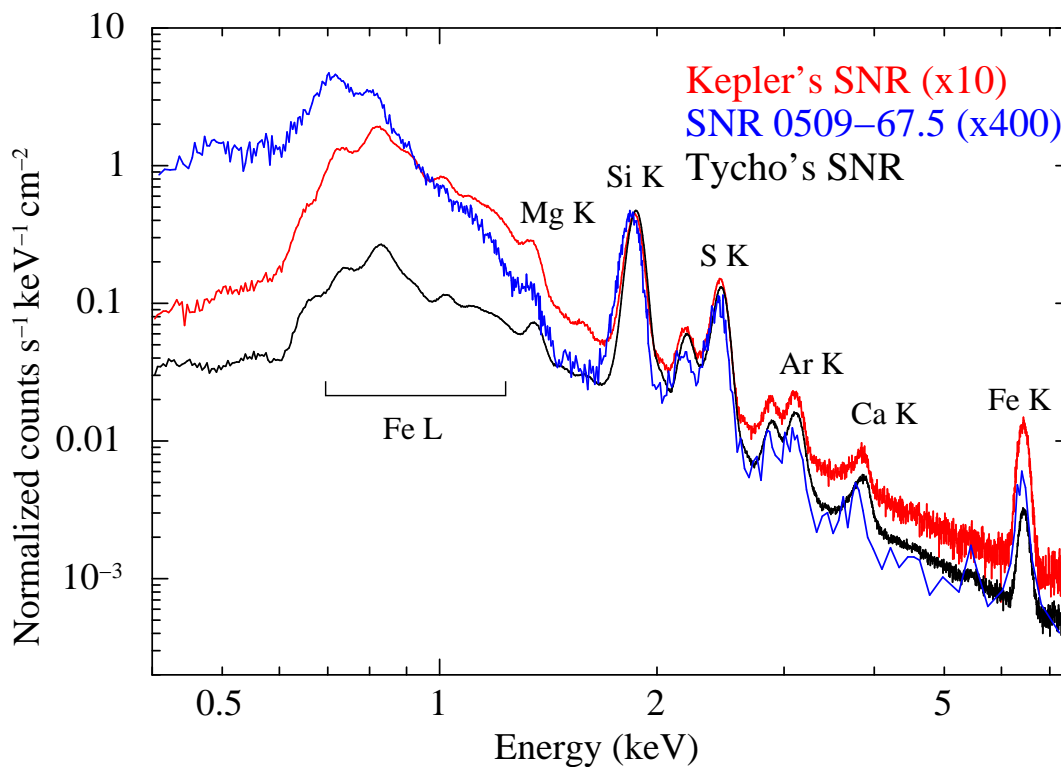


Fig. 1.— *Suzaku* XIS spectra of Kepler’s SNR in red, Tycho’s SNR in black, and SNR 0509-67.5 in blue. The intensities are normalized such that the peak values of Si K-shell lines are equalized. The error bars are omitted for clarity. The Fe L and Fe K lines for Kepler’s SNR and SNR 0509-67.5 are clearly stronger than those of Tycho’s SNR. It should be noted that these spectra are raw data, and are not corrected for the interstellar absorption.

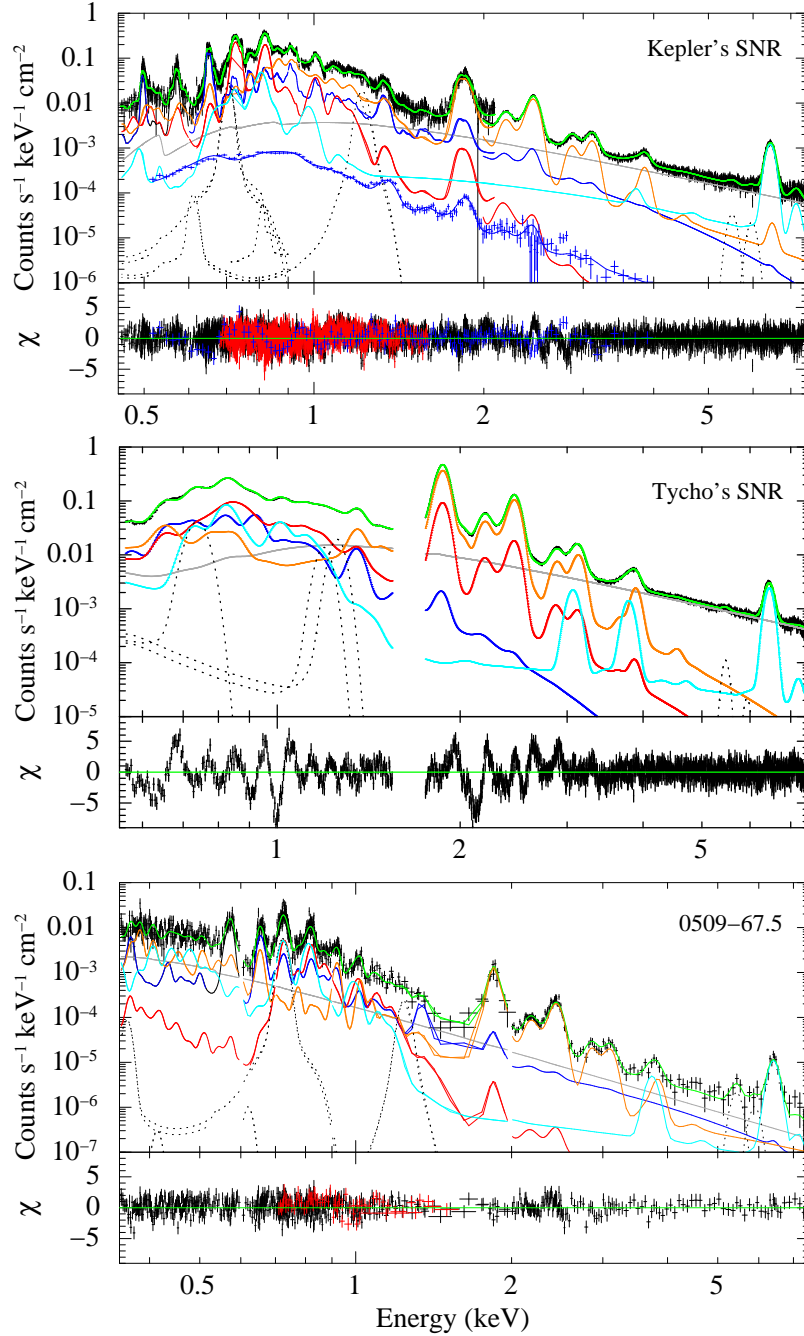


Fig. 2.— Spatially integrated X-ray spectra for Kepler’s SNR (upper panel), Tycho’s SNR (middle panel), and SNR 0509-67.5 (lower panel). We use the *XMM-Newton* RGS below 2 keV and the *Suzaku* XIS above 2 keV for both Kepler’s SNR and SNR 0509-67.5, but only the *Suzaku* XIS for Tycho’s SNR. For Kepler’s SNR, we simultaneously fit the *Chandra* ACIS spectrum extracted from the CSM knots (Knots 1 and 2 in Fig. 7). The lower panels show residuals. Individual components, i.e., swept-up, three ejecta, and power-law, are separately shown in blue, red+orange+light blue, and gray, respectively.

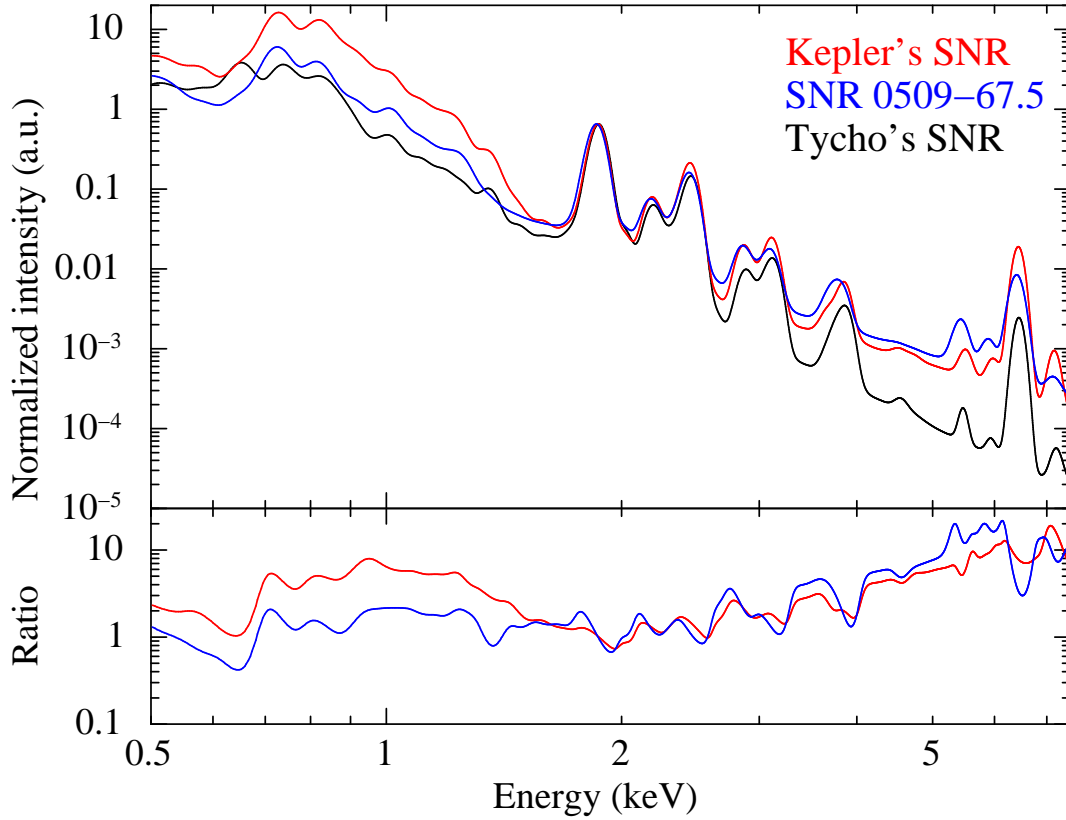


Fig. 3.— Comparison of unabsorbed ejecta emission models for Kepler’s SNR in red, SNR 0509-67.5 in blue, and Tycho’s SNR in black. The models are convolved with the XIS response function, and the intensities are normalized such that the peaks of Si K-shell lines are equalized. The lower panel shows spectral ratios with respect to Tycho’s SNR.

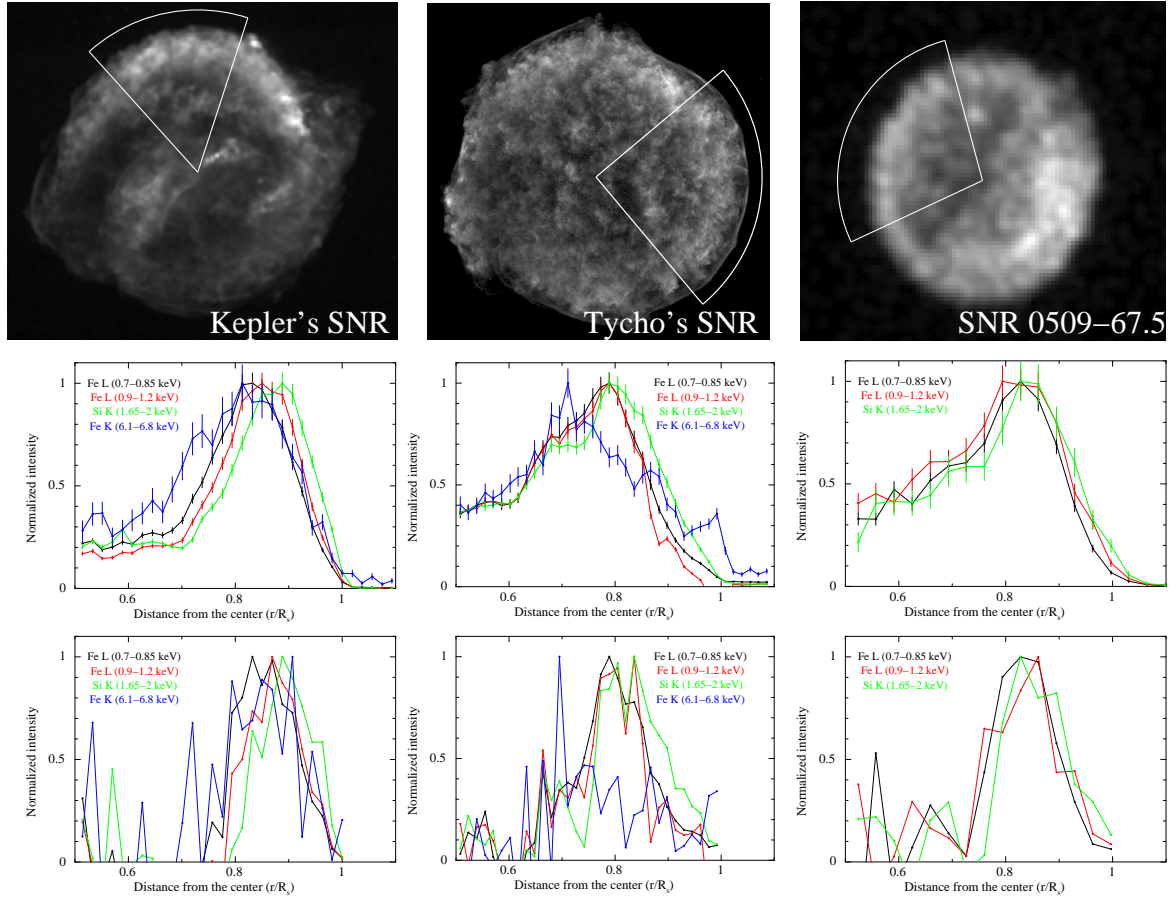


Fig. 4.— Top panels: *Chandra* ACIS images of the three SNRs analyzed in this paper. We extract radial profiles from the white pie-shaped areas covering relatively smooth, limb-brightened regions. Middle panels: X-ray radial profiles from the pie-shaped regions in top panels. The profiles are generated in four different energy bands: 0.7–0.85 keV (black), 0.9–1.2 keV (red), 1.65–2.0 keV (green), and 6.1–6.8 keV (blue). Bottom panels: Deprojected radial profiles corresponding to the profiles in the middle panel.

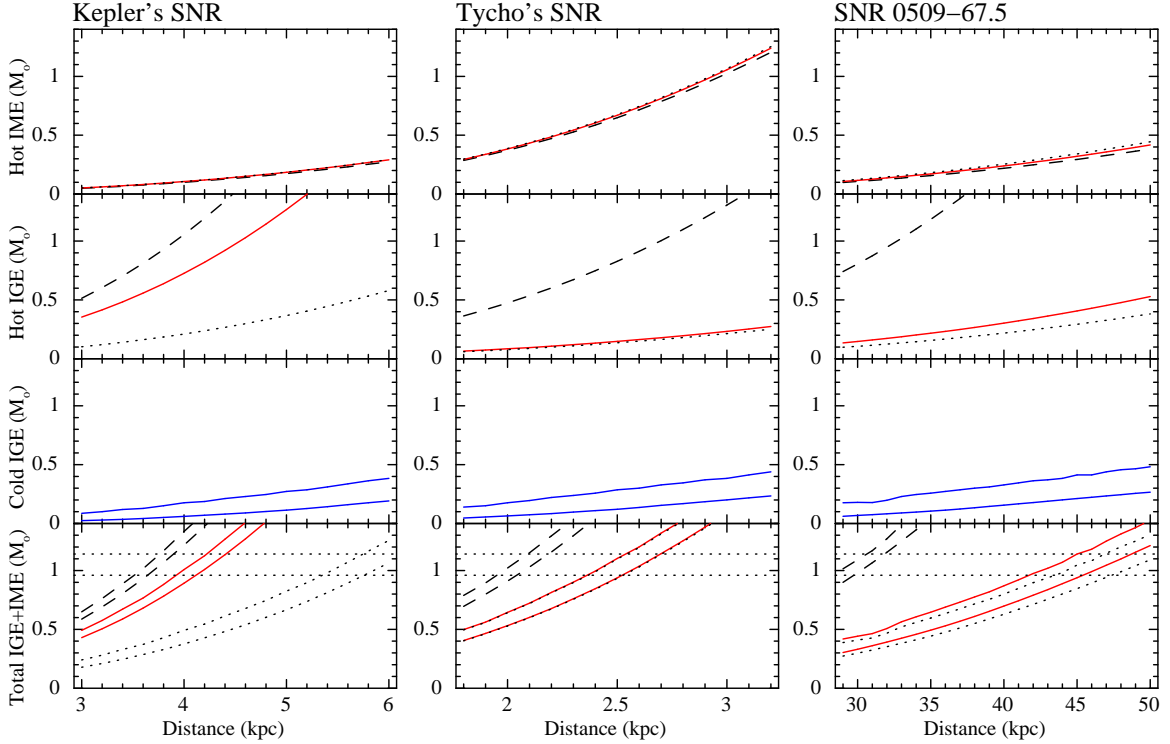


Fig. 5.— Ejecta masses as a function of distances to Kepler’s SNR (left column), Tycho’s SNR (central column), and SNR 0509-67.5 (right column). The top-row, second-row, third-row, and the bottom-row displays masses for shocked IME (Si+S+Ar+Ca), shocked IGE (Fe+Ni), unshocked IGE, and their sum, respectively. The dashed and dotted curves are obtained by fixing the electron temperature of the Fe-K emitting plasma at 2 keV and 15 keV, respectively, whereas solid red curves are responsible for the best-fit results. The cold IGE masses are based on two nucleosynthetic models, i.e., W7 (the upper curve: Nomoto et al. 1984) and O-DDT (the lower curve: Maeda et al. 2010). These two cases result in the pairs of curves in the bottom panel. In the bottom panels, the horizontal lines indicate the range of 0.96–1.14  $M_{\odot}$  Mazzali et al. (2007).

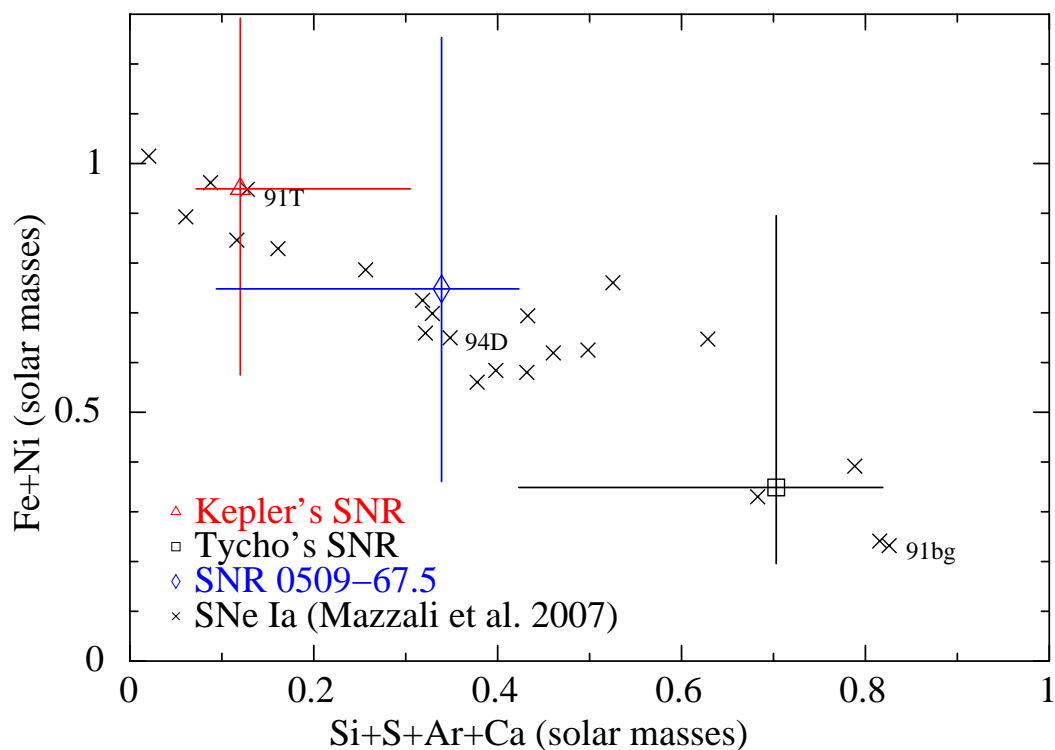


Fig. 6.— IGE masses vs. IME masses for 23 extragalactic SNe Ia (crosses: Mazzali et al. 2007). The data include a variety of subclasses of SNe Ia, i.e., overluminous (e.g., SN 1991T), normal (e.g., SN 1994D), and subluminous (e.g., SN 1991bg). Our data for Kepler’s SNR, Tycho’s SNR, and SNR 0509-67.5 are shown as a red triangle, a black box, and a blue diamond, respectively. The errors quoted are taken from Table 3.

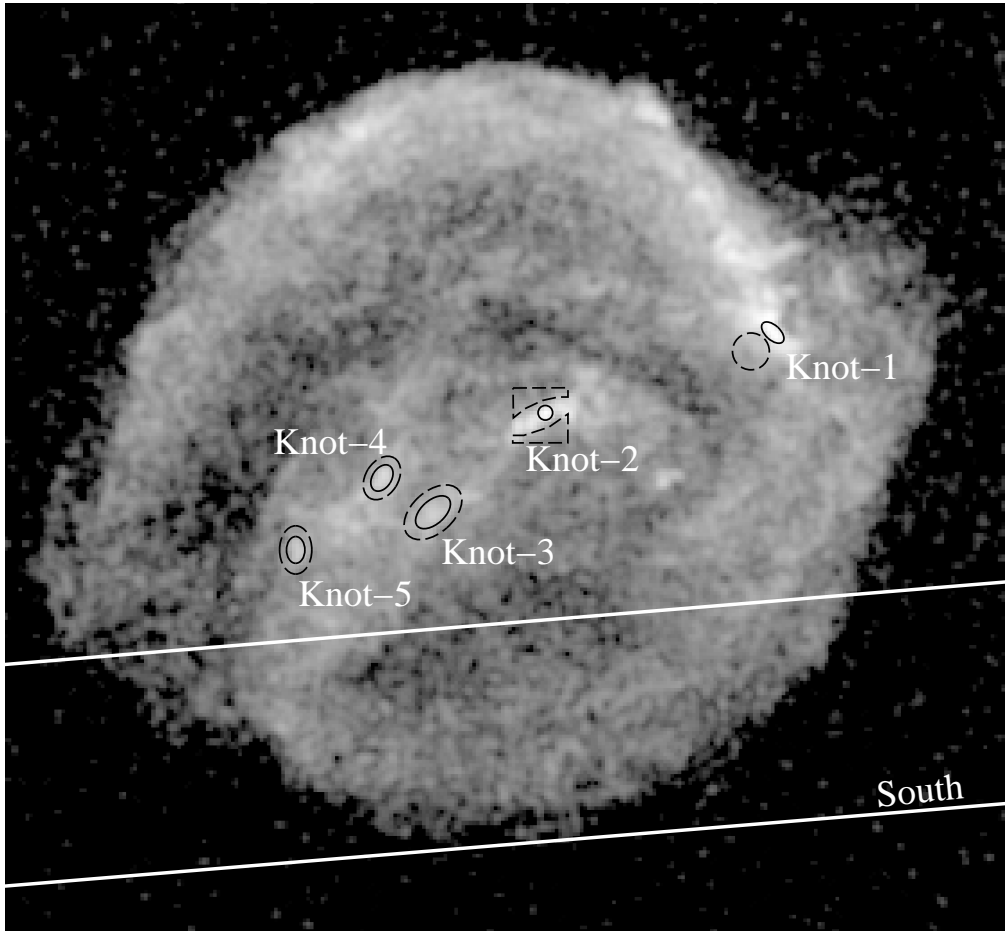


Fig. 7.— Spectral extraction regions for spatially-resolved CSM studies in Kepler’s SNR. For the diffuse CSM region, we extract the *XMM-Newton*’s RGS and *Chandra*’s ACIS spectra from the region within two white lines. For the CSM knots, we extract *Chandra*’s ACIS spectra from a solid circle and four solid ellipses. Dashed regions are where we extract local BGs.

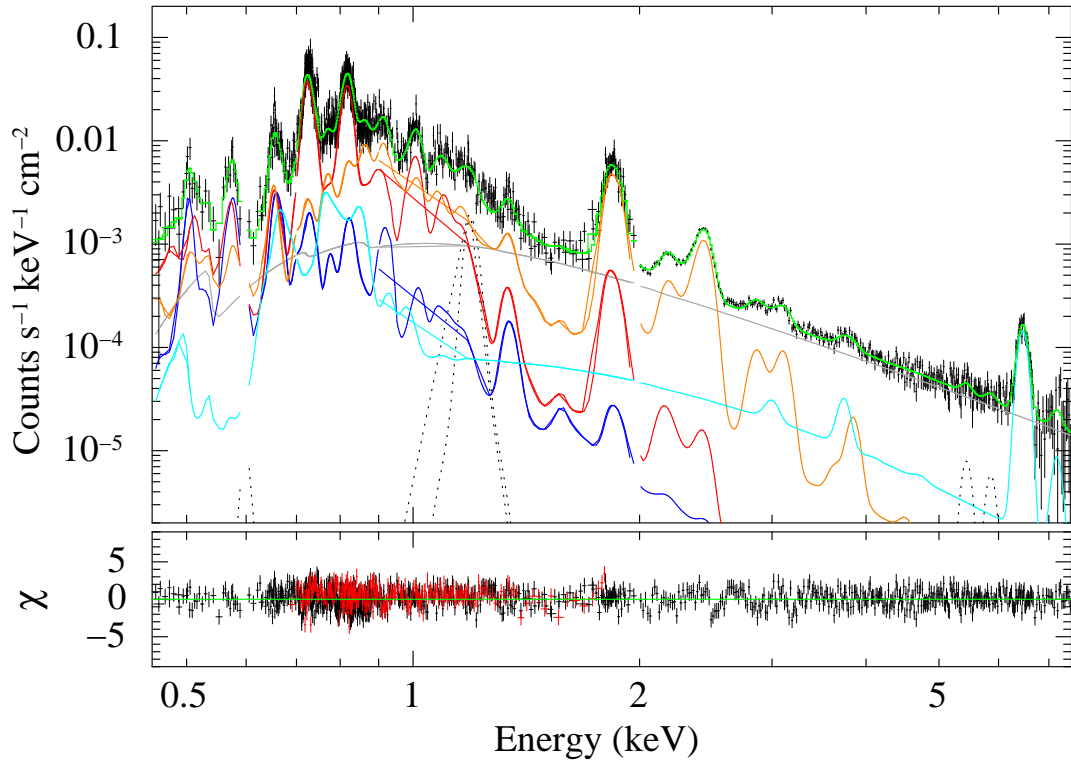


Fig. 8.— The combined RGS (below 2 keV) and the *Chandra*'s ACIS (above 2 keV) spectrum extracted from the southern portion of Kepler's SNR as shown in Fig. 7. The spectrum is fitted with the same model as we applied to the integrated spectra in Fig. 2. The lower panels show residuals.

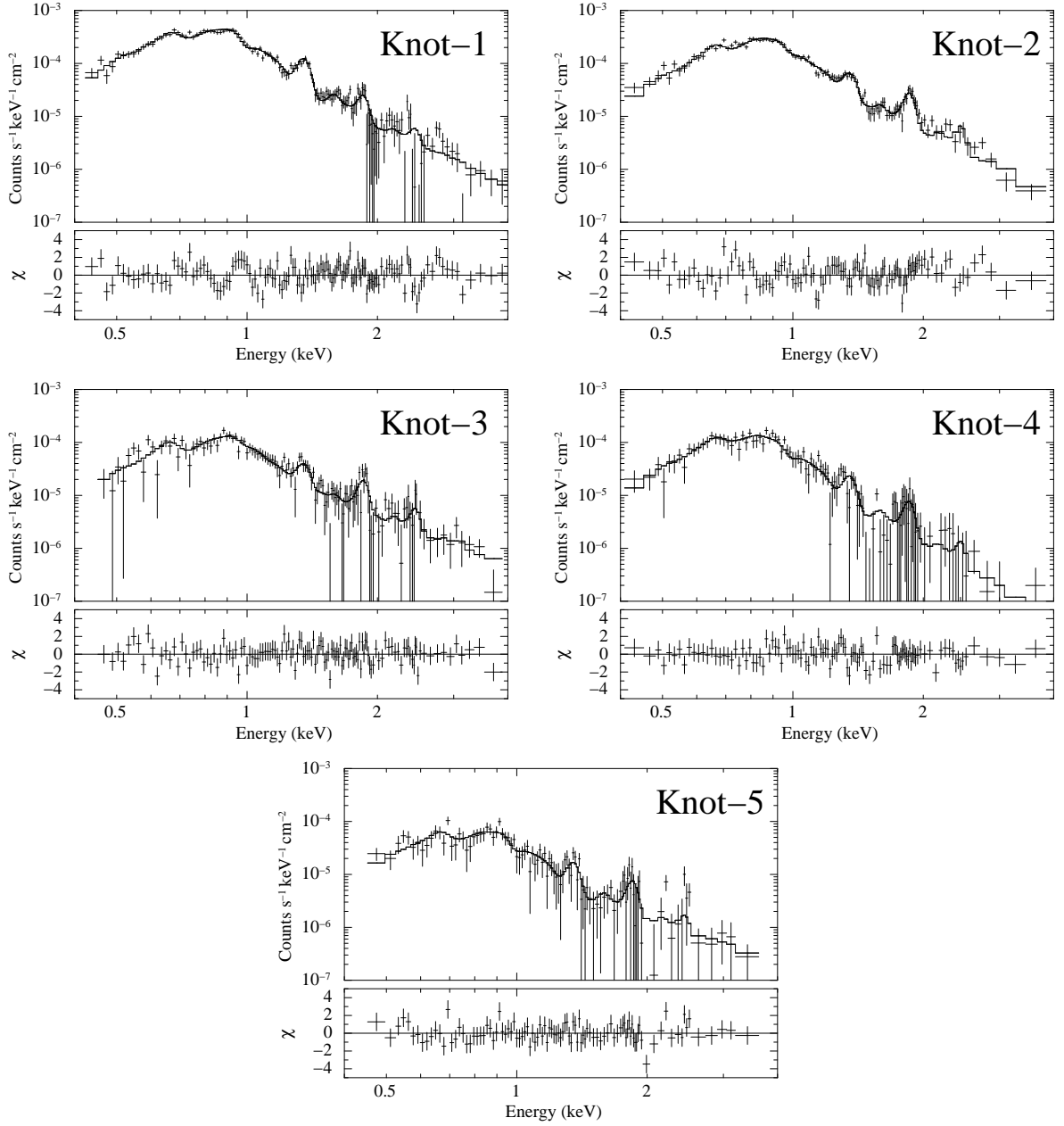


Fig. 9.— Local-BG subtracted *Chandra*'s ACIS spectra for CSM knots as shown in Fig. 7. The spectra are fitted with a single-component *vps shock* model. The lower panels show residuals.

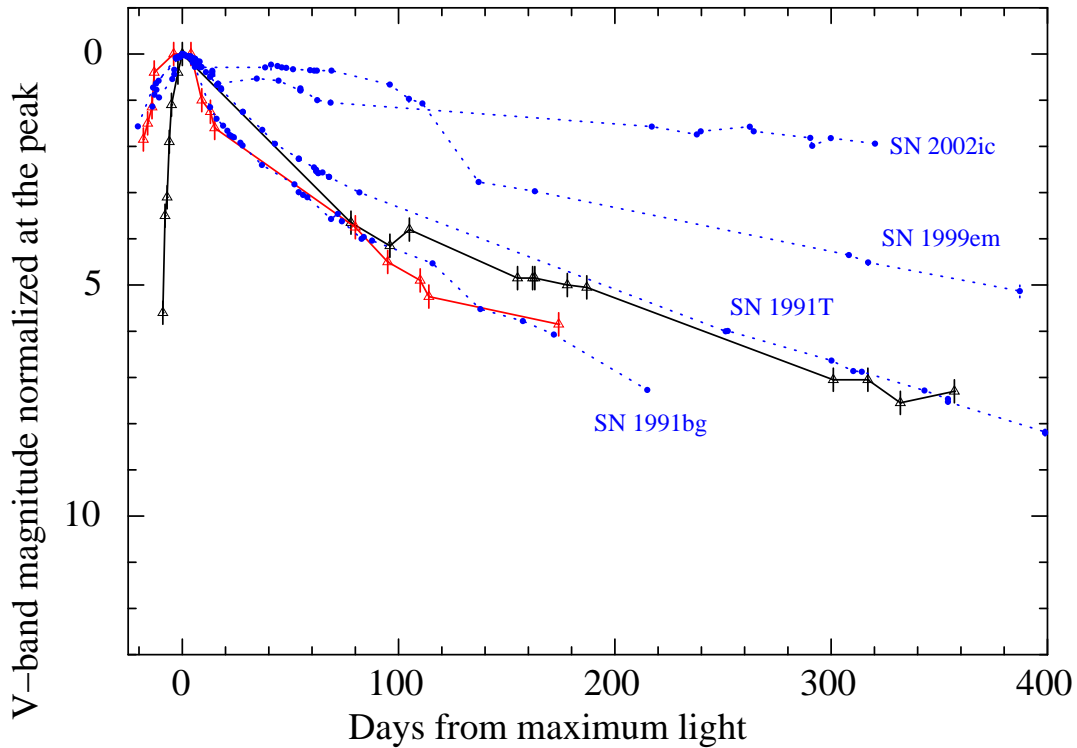


Fig. 10.— Light curves of Kepler’s SN and other modern SNe. The triangular data points in black and red tied by solid lines are responsible for Kepler’s SN, obtained by European and Korean observers, respectively. The errors are assumed to be  $\pm 0.25$  mag (Baade 1943). Other filled-circle data tied by dotted lines are responsible for recent SNe including Ia-CSM (SN 2002ic), 91T-like (SN 1991T), 91bg-like (SN 1991bg), and Type Iip (SN 1999em).

Table 1. X-ray data used in this paper

Target	Instrument	Obs. ID	Obs. Date	Effective exposure (ks)
Kepler’s SNR	<i>XMM-Newton’s</i> RGS	0084100101	2001-03-10	32.6
Kepler’s SNR	<i>Chandra’s</i> ACIS	6715	2006-08-03	159.1
Kepler’s SNR	<i>Suzaku’s</i> XIS	505092040	2011-02-28	146.2
Tycho’s SNR	<i>Suzaku’s</i> XIS	500024010	2006-06-27	101.1
SNR 0509-67.5	<i>XMM-Newton’s</i> RGS	0111130201	2000-07-04	36.0
SNR 0509-67.5	<i>Suzaku’s</i> XIS	508072010	2013-04-11	175.9

Note. — The PIs of the data are A. Decourchelle (Kepler - XMM), S. Reynolds (Kepler - Chandra), S. Park (Kepler - Suzaku), Suzaku science working group (Tycho - Suzaku), M. Watson (SNR 0509-67.5 - XMM), and H. Yamaguchi (SNR 0509-67.5 - Suzaku).

Table 2. Spectral-fit parameters for the integrated X-ray spectra

Parameter		Kepler's SNR	Kepler's SNR (south)	Tycho's SNR	SNR 0509-67.5
<b>CSM component</b>					
$kT_e$ (keV)		$1.06 \pm 0.03$	$0.48^{+0.57}_{-0.20}$	$0.41 \pm 0.01$	$1.76^{+0.85}_{-0.48}$
$\log(n_e t / \text{cm}^{-3} \text{ sec})$		$10.81^{+0.02}_{-0.01}$	$10.65^{+0.39}_{-0.17}$	$10.69^{+0.01}_{-0.05}$	$10.22^{+0.09}_{-0.34}$
Abundance <sup>a</sup> (solar)	N	$3.31^{+0.24}_{-0.25}$	$6.08^{+3.17}_{-2.75}$	1 <sup>b</sup>	$0.135^b$
Redshift ( $10^{-3}$ )		$1.39 \pm 0.05$	=Ejectal	=Ejectal	=Ejectal
Line broadening (E/1 keV eV)		$2.91^{+0.36}_{-0.32}$	=Ejectal	=Ejectal	=Ejectal
$\int n_e n_H dV / 4\pi d^2$ ( $10^{10} \text{ cm}^{-5}$ )		$193.15^{+4.03}_{-6.48}$	$9.37^{+11.11}_{-2.11}$	$1788.32^{+74.61}_{-12.55}$	$1.55^{+0.14}_{-0.43}$
<b>Ejecta components</b>					
1 $kT_e$ (keV)		$0.37 \pm 0.01$	$0.44^{+0.01}_{-0.02}$	$0.70^{+0.02}_{-0.01}$	$1.09^{+0.11}_{-0.24}$
$\log(n_e t / \text{cm}^{-3} \text{ sec})$		$10.52 \pm 0.01$	$10.39^{+0.06}_{-0.03}$	$10.79 \pm 0.01$	$10.14^{+0.02}_{-0.01}$
Abundance ( $10^4$ solar)	C	$0.54^b$	$0.54^b$	$0.54^b$	$0.54^b$
	N	$0^b$	$0^b$	$0^b$	$0^b$
	O	$0.25^{+0.02}_{-0.03}$	$0.31^{+0.12}_{-0.04}$	$0.75 \pm 0.01$	$0.22^{+0.3}_{-0.15}$
	Ne	$0.67^{+0.06}_{-0.07}$	$0.84^{+0.14}_{-0.16}$	$0(< 0.0003)$	$1.15^{+0.18}_{-0.17}$
	Mg	$0.77^{+0.07}_{-0.06}$	$0.53 \pm 0.14$	$0.34 \pm 0.01$	$0.07^{+0.30}_{-0.07}$
	Si	$10^b$	$10^b$	$10^b$	$10^b$
	S	$15.53^{+0.22}_{-0.14}$	$12.31^{+0.64}_{-0.66}$	$10.65^{+0.02}_{-0.03}$	$15.79^{+1.23}_{-0.94}$
	Ar	$18.98^{+0.46}_{-0.52}$	$11.34^{+1.69}_{-1.76}$	$11.02^{+0.07}_{-0.15}$	$10.59^{+2.16}_{-1.96}$
	Ca	$36.40^{+1.51}_{-1.60}$	$23.74^{+5.74}_{-5.62}$	$25.83^{+0.35}_{-0.50}$	$14.59^{+4.8}_{-2.46}$
	Fe	$13.65^{+0.17}_{-0.47}$	$6.63^{+2.58}_{-1.87}$	$1.49 \pm 0.01$	$175.56^{+1924.02}_{-56.18}$
$\int n_e n_H dV / 4\pi d^2$ ( $10^5 \text{ cm}^{-5}$ )		$961.42^{+114.02}_{-9.8}$	$230.29^{+104.58}_{-62.48}$	$9014.62^{+45.8}_{-775.91}$	$0.13^{+0.02}_{-0.04}$
Redshift ( $10^{-3}$ )		$-2.94 \pm 0.01$	$-5.60^{+1.84}_{-5.91}$	$-4.57 \pm 0.01$	$-0.89^{+0.23}_{-0.41}$
Line broadening (E/1 keV eV)		$9.13^{+0.14}_{-0.21}$	$10.16^{+0.48}_{-0.45}$	$9.90^{+0.05}_{-0.03}$	$11.90^{+0.78}_{-0.78}$
2 $kT_e$ (keV)		$2.08^{+0.01}_{-0.02}$	$1.46^{+0.33}_{-0.08}$	$0.96 \pm 0.01$	$5.44^{+0.82}_{-2.26}$
$\log(n_e t / \text{cm}^{-3} \text{ sec})$		$10.32 \pm 0.01$	=Ejectal	$10.90 \pm 0.01$	=Ejectal
Abundance <sup>c</sup> ( $10^4$ solar)	Fe	$3.58^{+0.04}_{-0.05}$	$2.23^{+0.15}_{-0.18}$	$0(< 0.0002)$	$0(< 0.03)$
$\int n_e n_H dV / 4\pi d^2$ ( $10^5 \text{ cm}^{-5}$ )		$875.35^{+4.73}_{-4.19}$	$131.51^{+21.9}_{-8.78}$	$22.75 \pm 0.02$	$0.013 \pm 0.001$
Redshift ( $10^{-3}$ )		=Ejectal	=Ejectal	=Ejectal	=Ejectal
Line broadening (E/1 keV eV)		=Ejectal	=Ejectal	=Ejectal	=Ejectal
3 $kT_e$ (keV)		$2.59 \pm 0.01$	$1.92 \pm 0.1$	$9.34^{+0.03}_{-0.25}$	$6.97^{+1.7}_{-1.08}$
$\log(n_e t / \text{cm}^{-3} \text{ sec})$		$9.21^{+0}_{-0}$	$9.02^{+0.04}_{-0.03}$	$9.80 \pm 0.01$	$9.60^{+0.05}_{-0.02}$
Abundance <sup>d</sup> ( $10^4$ solar)	Ar	$0 (< 0.19)$	$0.45^{+0.46}_{-0.43}$	$0 (< 2.7)$	$37.61^{+1.40}_{-1.09}$
	Ca	$1.43^{+0.31}_{-0.28}$	$1.65^{+0.59}_{-0.58}$	$64.82^{+1.69}_{-1.75}$	$47.28^{+16.22}_{-14.14}$
	Fe	$10^b$	$10^b$	$10^b$	$10^b$
Redshift ( $10^{-3}$ )		$-5.73^{+0.14}_{-0.18}$	$-9.50^{+0.98}_{-1.09}$	$-5.24^{+0.06}_{-0.05}$	$0.32^{+2.72}_{-1.08}$
Line broadening (E/1 keV eV)		$12.10 \pm 0.27$	$11.15^{+1.31}_{-1.42}$	$10.76^{+0.23}_{-0.24}$	$16.81^{+1.41}_{-1.34}$
$\int n_e n_H dV / 4\pi d^2$ ( $10^5 \text{ cm}^{-5}$ )		$5808.47^{+71.11}_{-63.17}$	$1748.80^{+137.58}_{-561.66}$	$1.08 \pm 0.01$	$0.006^{+0.002}_{-0.001}$
<b>Power-law component</b>					
$\Gamma$		$2.64^{+0.02}_{-0.01}$	$2.55^{+0.02}_{-0.01}$	$2.56 \pm 0.01$	$3.37^{+0.16}_{-0.2}$
Norm (ph keV <sup>-1</sup> cm <sup>-2</sup> s <sup>-1</sup> at 1 keV)		$98.93^{+5.51}_{-1.97}$	$24.49^{+0.43}_{-0.36}$	$714.68^{+1.96}_{-1.75}$	$1.85^{+0.37}_{-0.48}$
<b>Additional lines</b>					
Fe L+O K	Center (keV)	$0.708^{+0.002}_{-0.001}$	—	$0.741 \pm 0.001$	$0.724 \pm 0.002$
	Norm ( $10^{-4}$ ph keV <sup>-1</sup> cm <sup>-2</sup> s <sup>-1</sup> )	$68.18^{+5.4}_{-5.0}$	—	$986.88 \pm 19.1$	$2.38 \pm 0.3$
Fe L+Ne K	Center (keV)	—	$1.201 \pm 0.011$	$1.194^{+0.001}_{-0.003}$	—
	Norm ( $10^{-4}$ ph keV <sup>-1</sup> cm <sup>-2</sup> s <sup>-1</sup> )	—	$1.96^{+0.5}_{-0.4}$	$33.89 \pm 0.6$	—
Fe L+Ne K	Center (keV)	$1.227^{+0.001}_{-0.003}$	—	$1.254 \pm 0.001$	$1.244 \pm 0.001$
	Norm ( $10^{-4}$ ph keV <sup>-1</sup> cm <sup>-2</sup> s <sup>-1</sup> )	$22.75^{+1.2}_{-1}$	—	$42.40 \pm 0.5$	$0.19 \pm 0.1$
Cr K	Center (keV)	$5.514^{+0.035}_{-0.037}$	$5.438^{+0.073}_{-0.08}$	$5.474^{+0.016}_{-0.019}$	$5.436^{+0.068}_{-0.071}$
	Norm ( $10^{-7}$ ph keV <sup>-1</sup> cm <sup>-2</sup> s <sup>-1</sup> )	$85.18^{+16.7}_{-17.1}$	$17.96 \pm 10.2$	197.98	$7.05 \pm 3.2$
Mn K	Center (keV)	$5.976^{+0.04}_{-0.042}$	$5.862^{+0.266}_{-0.152}$	$5.935^{+0.07}_{-0.071}$	$5.893^{+0.068}_{-0.071}$
	Norm ( $10^{-7}$ ph keV <sup>-1</sup> cm <sup>-2</sup> s <sup>-1</sup> )	$60.18 \pm 16.3$	$14.16^{+10.8}_{-14.2}$	$41.07 \pm 32$	$3.56 \pm 3.4$
$\chi^2/\text{d.o.f.}$		8289.8 / 5724	1744.2 / 1305	5659.0 / 1981	1031.6 / 783

Note. —  $N_H$  values are fixed to  $6.4 \times 10^{21} \text{ cm}^{-2}$ ,  $1 \times 10^{22} \text{ cm}^{-2}$ , and  $0.6 \times 10^{21} \text{ cm}^{-2}$  for Kepler's SNR, Tycho's SNR, and SNR 0509-67.5, respectively. <sup>a</sup>Other elements are fixed to either the solar values (Wilms et al. 2000) or typical ISM values of the Large Magellanic Clouds (Korn et al. 2002; Russell & Dopita 1992) for the two Galactic SNRs or SNR 0509-67.5, respectively. <sup>b</sup>Fixed values. <sup>c</sup>Other elemental abundances are lined to those in the Ejectal component. <sup>d</sup>Other elemental abundances are fixed to zero.

Table 3. Ejecta masses ( $M_{\odot}$ )

Element	Kepler’s SNR	Tycho’s SNR	SNR 0509-67.5
O	$0.015^{+0.054}_{-0.008}$	$0.319^{+0.012}_{-0.159}$	$0.034^{+0.001}_{-0.018}$
Ne	$0.007^{+0.011}_{-0.004}$	$0(< 0.001)$	$0.033^{+0.002}_{-0.023}$
Mg	$0.002(< 0.005)$	$0.008^{+0.001}_{-0.005}$	$0.001(< 0.002)$
Si	$0.040^{+0.060}_{-0.014}$	$0.284^{+0.053}_{-0.123}$	$0.106^{+0.026}_{-0.072}$
S	$0.047^{+0.072}_{-0.016}$	$0.229^{+0.042}_{-0.096}$	$0.126^{+0.031}_{-0.090}$
Ar	$0.012^{+0.022}_{-0.006}$	$0.072^{+0.009}_{-0.024}$	$0.018^{+0.006}_{-0.011}$
Ca	$0.021^{+0.031}_{-0.012}$	$0.118^{+0.012}_{-0.041}$	$0.089^{+0.021}_{-0.072}$
Fe (shocked)	$0.710^{+0.094}_{-0.249}$	$0.134^{+0.387}_{-0.028}$	$0.372^{+0.355}_{-0.118}$
Ni <sup>a</sup> (shocked)	$0.110^{+0.015}_{-0.038}$	$0.021^{+0.060}_{-0.005}$	$0.058^{+0.055}_{-0.019}$
IGE <sup>b</sup> (unshocked)	$0.129^{+0.234}_{-0.087}$	$0.194^{+0.099}_{-0.120}$	$0.318^{+0.095}_{-0.250}$

Note. — <sup>a</sup>The Ni/Fe abundance ratio is assumed to be that expected in the W7 model (Nomoto et al. 1984). <sup>b</sup>Taken from the cold IGE panels in Fig. 5.

Table 4. Spectral-fit parameters for the CSM knots in Kepler’s SNR

Parameter	Knot-1	Knot-2	Knot-3	Knot-4	Knot-5
$kT_e$ (keV)	$1.10 \pm 0.11$	$0.95^{+0.1}_{-0.08}$	$1.92^{+0.57}_{-0.38}$	$0.68^{+0.13}_{-0.09}$	$1.84^{+0.97}_{-0.52}$
$\log(n_e t / \text{cm}^{-3} \text{ sec})$	$10.59^{+0.07}_{-0.09}$	$10.96^{+0.13}_{-0.12}$	$10.66^{+0.09}_{-0.12}$	$10.91^{+0.19}_{-0.17}$	$10.36^{+0.2}_{-0.18}$
Abundance (solar)	N	3.5 <sup>a</sup>	3.5 <sup>a</sup>	3.5 <sup>a</sup>	3.5 <sup>a</sup>
	O	$0.97^{+0.15}_{-0.13}$	$0.95^{+0.21}_{-0.08}$	1	1
	Ne	$1.31^{+0.23}_{-0.22}$	$0.84^{+0.22}_{-0.21}$	1	1
	Mg	$1.43^{+0.2}_{-0.18}$	$0.91^{+0.16}_{-0.15}$	1	1
$\int n_e n_H dV / 4\pi d^2$ ( $10^{10} \text{ cm}^{-5}$ )	$1.87^{+0.17}_{-0.15}$	$1.58 \pm 0.13$	$0.55^{+0.06}_{-0.05}$	$0.77^{+0.14}_{-0.12}$	$0.26^{+0.03}_{-0.02}$
$n_e$ ( $\text{cm}^{-3}$ )	23.4	29.2	6.4	11.3	6.9
Mass ( $10^{-4} M_{\odot}$ )	2.8	1.9	3.1	2.4	1.3
$\chi^2/\text{d.o.f.}$	181.8 / 134	163.1 / 111	130.1 / 128	95.9 / 109	95.6 / 101

Note. —  $N_H$  values are fixed to  $6.4 \times 10^{21} \text{ cm}^{-2}$ . We assume  $n_e = 1.2n_H$  and the distance  $d = 4.2 \text{ kpc}$ .  
<sup>a</sup>Fixed values.